

Interface Stability During Rapid Solidification of Silicon-Tin

A thesis presented

by

David Eric Høglund

to

The Division of Applied Sciences

in partial fulfillment of the requirements

for the degree of

Doctor of Philosophy

in the subject of

Applied Physics

Harvard University

Cambridge, Massachusetts

February 1996

© 1996 by David Eric Høglund

All rights reserved.

## ABSTRACT

Rapid solidification conditions significantly enhance the stability of the solid-liquid interface. At sufficiently high velocities, the stabilizing effect of capillarity is augmented by nonequilibrium effects. For example, solute trapping allows incorporation of solute at concentrations higher than equilibrium and therefore reduces constitutional supercooling in the liquid ahead of the interface. Recent interface stability theories have taken nonequilibrium solidification effects into account in a coherent and thermodynamically consistent way. The quantitative measurements presented here confirm the predictions about the limit of interface stability in velocity-concentration space for directional solidification of a dilute solution far from equilibrium.

If the interface conditions are uniform and constant, the solid formed will also be uniform and constant, therefore a solid solution. The onset of microsegregation marks the limit of interface stability. The samples used for the experiment were silicon and silicon-on-sapphire (SOS) wafers implanted with tin. The SOS samples were also photolithographically patterned for transient conductance measurements. Pulsed laser melting by XeCl excimer, ruby, and Nd:YAG lasers permitted solidification velocities from 1 to 10 m/s. Velocities for the SOS samples were calculated from transient conductance measurements. For the bulk silicon samples, velocities were determined from heat flow calculation calibrated against reflectance measurements (time) and cross-sectional electron microscopy of samples with a boron marker at the maximum melt depth (distance). Rutherford backscattering spectrometry, ion channeling measurements, and electron microscopy were used to determine the critical concentration for interface breakdown. For a (100)-oriented sample solidified at 3 m/s, the interface might undergo breakdown at 0.3 atomic percent tin, resulting in a cellular structure with a cell size of order 600 Å. The critical concentration is therefore three times the maximum equilibrium solubility and thirty times what a theory assuming local equilibrium would predict. Measurements for (111)-oriented samples also agree with theory.

Quantitative solute trapping measurements for the (100) orientation are well fit by a liquid diffusivity of  $2.5 \times 10^{-4}$  cm<sup>2</sup>/s and by the continuous growth model with a diffusive velocity of 17 m/s.

repaginated version

# CONTENTS

1 Introduction .....	1
1.1 Local Equilibrium Theories .....	4
1.2 Nonequilibrium Solidification Theory.....	13
1.3 Nonequilibrium Stability Theory.....	16
1.4 Previous Experiments.....	27
2 Experimental Methods.....	31
2.1 Choice of Alloy System.....	31
2.2 Sample Preparation .....	34
2.3 Experimental Setup .....	36
2.4 Relation Between Theory and Experiment.....	44
3 Interpretation of Data.....	47
3.1 Ion Scattering .....	47
3.2 Electron Microscopy.....	56
3.3 Measurement of Melt Duration.....	62
3.4 Measurement of Velocity I: Transient Conductance.....	63
3.5 Measurement of Velocity II: Microscopy and Simulations .....	67
4 Solute Trapping in Silicon-Tin.....	85
5 Interface Stability in Silicon-Tin.....	91
5.1 SOS .....	91
5.2 Bulk Silicon Samples: (100) Orientation.....	102
5.3 RBS Analysis of Breakdown: Nd:YAG Laser .....	132
5.4 Bulk Silicon Samples: (111) Orientation.....	135
5.5 Bulk Silicon Samples: Cell Size .....	144
Chapter 6 .....	146
Appendices	
Appendix A: Modifications to SA .....	152
Appendix B: Silicon Properties used in Heat Flow Simulations.....	155
References.....	157

## FIGURES

1.1	Solute redistribution ahead of a curved interface .....	3
1.2	Spatial coordinates for analysis of directional solidification.....	4
1.3	Solvent side of equilibrium phase diagram for dilute solutions.....	5
1.4	Steady-state solute profile during directional solidification .....	6
1.5	Temperature profile and liquidus temperature in liquid.....	7
1.6	Spatial coordinates for Mullins-Sekerka analysis.....	8
1.7	Amplification rate as a function of perturbation wavenumber for Mullins-Sekerka analysis.....	11
1.8	Neutral stability curve for Mullins-Sekerka analysis.....	12
1.9	Solvent side of nonequilibrium phase diagram for dilute solutions	16
1.10	Neutral stability curve for Coriell-Sekerka analysis .....	17
1.11	Neutral stability curve for Merchant-Huntley-Davis analysis .....	18
1.12	Neutral stability curve for silicon-tin calculated by Huntley and Davis.....	21
1.13	Neutral stability curve for silicon-tin calculated by Brunco.....	26
2.1	Generalized setup for pulsed laser melting .....	36
2.2	Generalized setup for measuring surface reflectivity.....	37
2.3	Generalized setup for measuring sample conductance.....	37
2.4	Mask for patterning samples for conductance measurements.....	38
2.5	Average temporal profile of XeCl excimer laser at Harvard.....	40
2.6	Pulsed laser melting setup at Sandia National Laboratory.....	41
2.7	Pulsed laser melting setup at Cornell University.....	41
2.8	Spatial intensity profile for Nd:YAG laser at Cornell University.....	42
2.9	Typical temporal profiles for Nd:YAG laser at Cornell University...	43
2.10	Average temporal profile for Nd:YAG laser at Cornell University..	43
2.11	Trajectory of an experiment through concentration-velocity space..	45
3.1	Geometry for ion scattering measurements .....	48
3.2	Evolution of solute distribution during pulsed laser melting.....	51
3.3	Axial channeling of an ion beam.....	52
3.4	Aligned and random ion channeling spectra for pure silicon and silicon-tin.....	54
3.5	Effect of finite detector resolution on ion channeling spectra.....	55

3.6	Recipe for making cross-sectional TEM samples .....	56
3.7	Cut-away view of a sample that under-went cellular breakdown ....	57
3.8	Scanning transmission electron microscope set up for Z-contrast imaging.....	57
3.9	Role of camera length in Z-contrast imaging .....	60
3.10	Typical measurement of bulk silicon surface reflectivity .....	63
3.11	Typical measurement of bulk silicon conductance .....	66
3.12	First order approximation to solidification velocity .....	68
3.13	Improved approximation to solidification velocity.....	69
3.14	Ion channeling spectrum of silicon implanted at room temperature	71
3.15	Heat flow simulations of silicon with an amorphous surface layer	73
3.16	Measured melt duration as a function of laser fluence for various implants; twelve implants and constant tin.....	75
3.17	Measured melt duration as a function of laser fluence for other implants; constant boron and no boron.....	78
3.18	Heat flow simulations of silicon with a 1600Å amorphous layer on the surface.....	79
3.19	Comparison of simulated and measured solidification velocities...	81
3.20	Typical measurement of bulk silicon surface reflectivity showing interference from Nd:YAG pulse .....	83
4.1	Pulsed laser melting of a SOS sample.....	86
4.2	Fitting for the partition coefficient k.....	88
4.3	Fit of continuous growth model to silicon-tin partitioning data.....	90
5.1	Interface stability data for SOS: no indication of breakdown.....	93
5.2	Interface stability data for SOS: RBS and TEM analysis of breakdown.....	95
5.3	Regular and Z-contrast microscopy for a SOS sample .....	98
5.4	Analysis of cell wall lengths for a SOS sample .....	99
5.5	Interface stability data for SOS: RBS analysis of breakdown (no TEM) .....	101
5.6	RBS and channeling measurements of sample IS10-04-01.....	107
5.7	Electron micrographs of sample IS10-04-01 .....	109
5.8	RBS and channeling measurements of sample IS04-184 .....	111
5.9	RBS and channeling measurements of sample IS06-075 .....	113

5.10	Electron micrographs of samples (a) IS04-184 and (b) IS06-075.....	115
5.11	RBS and channeling measurements of sample IS03-247.....	117
5.12	RBS and channeling measurements of sample IS11-02-13.....	119
5.13	Electron micrographs of samples (a) IS03-247 and (b) IS11-02-13.....	121
5.14	RBS and channeling measurements of sample IS12-01-20.....	123
5.15	RBS and channeling measurements of sample IS12-02-08.....	125
5.16	Electron micrographs of samples (a) IS12-01-20 and (b) IS12-02-08.....	127
5.17	Interface stability data for bulk Si(100) melted with XeCl: RBS and TEM analysis of breakdown.....	128
5.18	Interface stability data for bulk Si(100) melted with XeCl: RBS analysis of breakdown (some TEM); solute gradient effect.....	131
5.19	Interface stability data for bulk Si(100) melted with Nd:YAG: RBS analysis of breakdown (one TEM sample).....	134
5.20	RBS and channeling measurements of sample 111-2-028.....	138
5.21	RBS and channeling measurements of sample 111-4-010.....	140
5.22	Electron micrographs of samples (a) 111-2-028.....	142
5.23	Interface stability data for bulk Si(111) melted with XeCl: RBS analysis of breakdown (two TEM samples).....	143
5.24	Plan-view TEM showing cellular structure.....	145
6.1	Comparison of measured and simulated solidification velocities....	149
6.2	Master plot of interface stability experiments in Si(100) .....	151

## TABLES

1.1	Symbols and definitions for stability theory .....	29
2.1	Inputs to calculation of silicon-tin interface stability.....	33
2.2	Ion implantation recipes .....	35
2.3	Spatial uniformity of excimer pulse measured by two-beam reflectivity.....	40
3.1	Solidification velocities for bulk silicon samples estimated using equation 3.11.....	69
3.2	Comparison of measured and simulated maximum melt depths ...	82
3.3	Solidification velocities for SOS sample estimated using equation 3.11.....	84
5.1	Interface stability data for SOS: no indication of breakdown.....	92
5.2	Interface stability data for SOS: RBS and TEM analysis of breakdown.....	94
5.3	Interface stability data for SOS: RBS analysis of breakdown (no TEM) .....	100
5.4	Interface stability data for bulk Si(100) melted with XeCl: RBS and TEM analysis of breakdown.....	105
5.5	Interface stability data for bulk Si(100) melted with XeCl: RBS analysis of breakdown (no TEM) .....	129
5.6	Interface stability data for bulk Si(100) melted with Nd:YAG: RBS analysis of breakdown (one TEM sample).....	133
5.7	Interface stability data for bulk Si(111) melted with XeCl: RBS and TEM analysis of breakdown .....	136



## ACKNOWLEDGMENTS

I had the good fortune to receive a project that had been started by competent hands. Mike Aziz started the project during his post-doc at ORNL SMAC; Sam Coriell helped Mike with first version of the cells program; Jeff Tsao, Paul Peercy, and Dick Blake shot SOS samples with the ruby lasers at Sandia (funded by DOE through DE-AC04-76DP00789); and Scott Stiffler, then a student at Cornell with Mike Thompson, did TEM on the SOS samples (funded by NSF-PYIA; J. Hurt). I spent my first summer at Harvard doing more microscopy on the SOS samples; Clive Hayzelden provided instruction in Z-contrast imaging. Early work at Harvard was funded by Sandia and the Harvard MRL (NSF-DMR-86-14003).

I finished coursework about the same time that Mike Aziz, my advisor, received the big DOE grant (DE-FG02-89ER45401, J.B. Darby). This grant supported me all the way through; when it was finished, I was finished. Mike kept me funded on a provocative and challenging experiment. Mike along with Frans Spaepen and David Turnbull have given materials science at Harvard its intellectual keenness. I admire the way these three think about science and put thoughts on paper; it is an honor to have them sign this work. Also among faculty, Chris Lobb provided crucial academic advising.

My interest in graduate school started when I was an undergraduate co-op student at Oak Ridge National Laboratory. The staff of the Hollefield facility and Surface Modification and Characterization facility showed me how science makes life fun. I made several trips to SMAC to do implants and RBS. Each time I returned with nice samples, good data, and renewed enthusiasm.

I also did parts of this thesis in Mike Thompson's laboratory at Cornell. I would have come home empty-handed without a lot of help from Mike Thompson and David Brunco. The trip also intensified my interaction with David. Our discussions clarified much of my thinking and helped me articulate the fine points of my thesis. David also did silicon-tin stability calculations for me. I have also benefited from the theory and visits to Harvard by Prof. Stephen Davis and Douglas Huntley.

In hindsight, the best reason for going to Harvard is to learn from one's peers. I will always look up to Kwang-Ryeol Lee for all that he taught me about experimental research. I also enjoyed the camaraderie within the laser lab: Jeff West, Nobuaki Isono, Riccardo Reitano, Jonah Erlebacher, and Jim McCamy. I worked countless hours shoulder to shoulder with Pat Smith whose thesis on solute trapping served as my primer on planar-interface solidification.

Beyond the walls of the laser lab, I have shared in the science, success, sufferings, and softball of my materials science friends: Bill Carter, Salman Mitha, Jim Ruud, Yan Shao, Alison Shull, Andrew Wagner, Ann Witvrouw, Howie Zolla, and many others. Glen Wilk's recipe for cross-sections ended one of my woes. Frans Spaepen has been of constant and warm encouragement. Among the staff, I am particularly indebted to David Carter in the clean room (chlorine RIE worked, but in the end polishing worked better), John Chervinsky in RBS, and Yuan Lu in the TEM lab (a constant help), and last but not least, Joe Bell whose retirement is a really good reason to finish now; when I grow up, I want to be like Joe.

I would especially like to acknowledge the people who have helped me write this thesis: Alison (my coach), David Brunco, Bill, and Jonah. Alison, Bill, Jonah, and Craig Arnold have kept the distance between me and the best of lab small.

The last seven years have been very rich. That I write my thesis in Paris is testimony enough. So far, I have talked only the web of friendships that have made the laser lab and McKay Lab my home. My years at Harvard would be much poorer without friends like Hans Guido, Julie Nucci, and Lung-Han Peng who weathered classes with me first year, and like Ann Ferentz (Chemistry), Ping-yu Hsu (EALC), Carol Tsang (HEAL), and the hundred or so men that I sang with in the Harvard Glee Club. Likewise, my time in Boston would be poorer without the abundant life and wind of the Spirit at University Lutheran Church. I am deeply indebted to my family and close friends for unfailing love and support. My staying in school through my mother's death is a tribute to the faith and love we share. Finally, a word of thanks to Susanna my love: this year has been one of the happiest of my life; you have been a help meet for this labor.

I thank all of you.

To the glory of God

Tu solus sanctus,  
Tu solus Dominus,  
Tu solus altissimus.



# Chapter 1

## Introduction

Consider what happens when a crystal grower in the semiconductor industry pulls an ingot of silicon from a crucible. A liquid metal becomes a solid semiconductor. Long-range order appears; the viscosity increases greatly, and the self-diffusivity decreases similarly. Yet both the liquid and the solid are silicon. The remarkable process that effects this transformation is solidification.

Consider another crucible of molten silicon. This time the melt is not pure, but has a second component dissolved in it, say tin (we are in the research laboratory now, not the semiconductor industry). In the liquid phase, the solubility of tin is large. There is total solubility at sufficiently high temperature. In the solid however, the solubility is quite low. Thus, solubility is another property that changes during solidification.

When pulling an ingot, it is usually assumed that solidification takes place at equilibrium. Strictly speaking however, there must be some deviation from equilibrium, for if the solid and liquid are in perfect equilibrium, then there will be no net attachment of solute or solvent to the interface. For example, a decrease in temperature will cause atoms in the liquid to attach to the solid. Thus interface velocity is related to solid-liquid interface temperature. And what about concentration? The phase rule assures

that the concentration of solute atoms attaching to the solid will not be exactly the same as the concentration in the melt. On the phase diagram, the width of the two-phase region is quantified in terms of a segregation coefficient. Its value will depend on temperature and velocity. All these quantities are interrelated. A change in either temperature, solute concentration, or velocity will cause a change in the other two quantities.

Solidification theory relates interface temperature, interface velocity, and solute concentrations on either side of the interface. A basic assumption is that for a given liquid, a specified set of interface conditions always creates the same solid. Thus if experimental factors can be controlled so that the interface conditions are uniform and constant, the solid will be uniform as well.

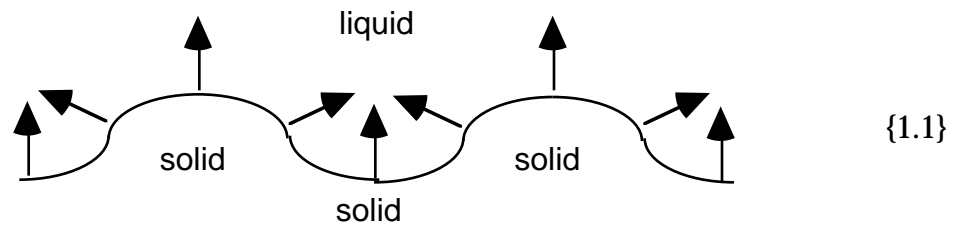
Experimental tests of solidification theory are never ideal. One can only imagine a system where the solvent is clear and the solute a dye, and an optical/thermal camera simultaneously monitors the interface position, solute distribution, and the thermal fields. In real life, one relies on a mix of measurements made before, during, and after solidification. Experimental tests of solidification theory using rapid solidification are especially interesting. The required high rate of heat removal assures that the solid spends little time at elevated temperatures. Thus the relation between interface conditions during solidification and solid observed afterwards is particularly close.

This thesis tests linear interface stability theory during rapid solidification. Energetic pulses from spatially homogeneous lasers melt a sample to a uniform depth. Solidification therefore begins with a planar solid-liquid interface. Proper sample preparation assures that the melt is uniform on any plane parallel to the interface, which in turn assures that the interface conditions are initially uniform. If the interface is stable, conditions stay uniform, and the result is a solid solution.

Stability theory considers what happens when the interface is perturbed. (Linear stability theory assumes that the perturbations are small enough that the effect of the perturbation is proportional to the size of the perturbation.) The perturbation causes effects that either oppose it or amplify

it. Effects that oppose the perturbation push the interface towards planarity, favoring uniform interface conditions and hence the growth of a solid solution. Effects that amplify the perturbation favor further growth of the perturbation, hence changing the interface shape. Lateral diffusion of heat and solute and a variety of solidification directions make for a variety of interface conditions. Various solids emerge.

The breakdown mode for silicon-tin is cellular, as illustrated in figure 1.1.



Rejection of solute along the direction of solidification, shown by arrows, causes solute (tin) to accumulate in the troughs of the perturbation. The accumulation of solute lowers the liquidus temperature in the troughs, delaying solidification and allowing even more solute to collect. Eventually the troughs are so rich in tin that the tin precipitates out of solution.

In summary, uniform interface conditions lead to a solid solution; non-uniformity leads to a cellular structure. Conversely, the microstructure of the resulting solid tells the history of the interface. Thus, this thesis has two parallel themes. The first is a test of linear stability theory combined with a particular model of solidification. The second is a phenomenological investigation of solid solubility. The two themes have a common focal point because the limit of interface stability is also the limit of solid solubility.

Although this thesis is restricted to directional solidification, systems operating at the point of marginal stability are of general interest [van Saarloos, 1988]. The dendrite problem [Langer and Müller-Krumbhaar, 1978] is closely related to directional solidification. Instead of the latent heat flowing away from the interface through the solid, it flows into the undercooled liquid. Theoretical studies of a protrusion growing into the liquid, a dendrite, predict a family of solutions characterized by a fixed ratio of tip velocity to tip radius. An early assumption that the experimentally observed shape would

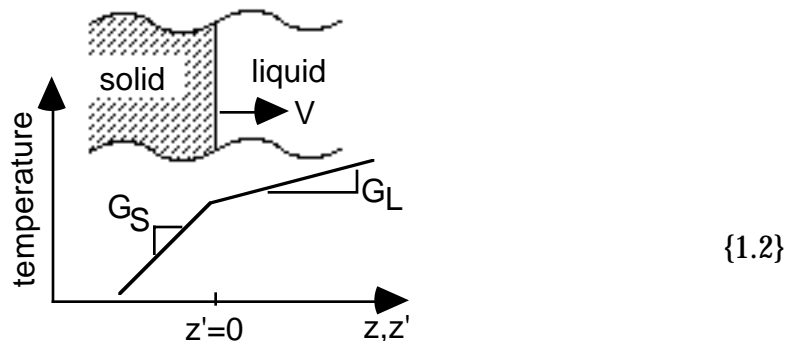
correspond to the solution with the highest velocity proved incorrect. Instead the measured tip velocity and tip radius correspond to the solution where the interface is marginally stable.

## 1.1 Local Equilibrium Theories

In the model experiment, one pulls a boat of liquid alloy out of a furnace at a constant rate (the pulling speed). Both the boat and furnace are infinitely long, so the system eventually reaches steady-state. Once the boat is away from the heat of the furnace, the melt begins to solidify, eventually reaching a velocity equal to the pulling speed. In the reference frame of the lab, the solid-liquid interface remains at a fixed position, the distance from the furnace being some function of the heat flow from boat to room. In a reference frame attached to the boat, the interface moves at a velocity opposite in sign but equal to the velocity at which the boat is pulled from the furnace.

### 1.1.1 Directional Solidification

Figure 1.2 shows a simple one-dimensional model of the experiment.



The melt solidifies as the solid-liquid interface moves from left to right. The temperature gradient in the liquid  $G_L$  and in the solid  $G_S$  are positive meaning that the heat in the melt and the latent heat released during solidification are removed through the solid. The interface is planar and moves at a fixed velocity,  $V$ , in the  $z$  direction. The primed coordinates move with the interface. In steady-state, the diffusion equations for solute and heat in the primed coordinate system appear constant. The problem is essentially one dimensional in that any quantity is constant on any plane parallel to the

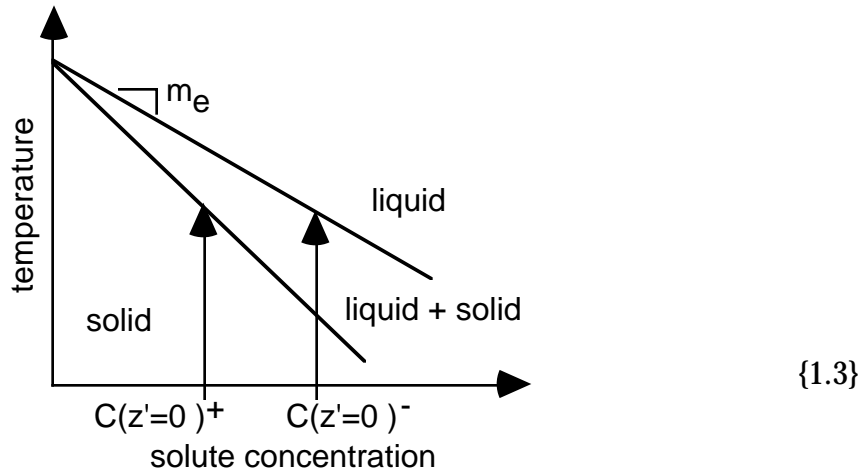
interface. Heat leaves the system through the solid, assuring a positive temperature gradient,  $G_L$ , in the liquid. For a pure melt, this condition is sufficient to insure that the interface remains planar.

### 1.1.2 Constitutional Supercooling (solute-driven instability)

The constitutional supercooling criterion of Tiller, Jackson, Rutter, and Chalmers [Tiller, Jackson, Rutter, and Chalmers, 1953] is the first quantitative description of interface stability for alloy solidification. The solute field is determined by diffusion in the liquid (diffusion in the solid and convection in the liquid are assumed negligible) and the partition coefficient

$$k = \frac{C(z'=0^-)}{C(z'=0^+)} \quad (1.1)$$

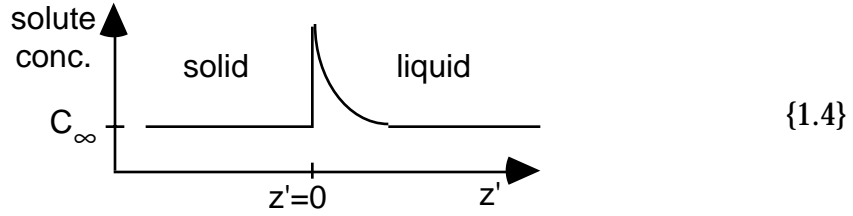
where the  $C$ 's are the concentration of solute at the interface in the solid ( $z' < 0$ ) and liquid ( $z' > 0$ ). In this version of the theory, the solid and liquid on either side of the interface are in local equilibrium, so  $k$  can be obtained from inspection of the equilibrium phase diagram. For dilute solutions, the solvent side of the phase diagram looks like figure 1.3.



Because this is an equilibrium phase diagram,  $k$  equals its equilibrium value  $k_e$ . Also,  $k_e$  is assumed constant and less than 1.0 so that the growing solid is rejecting solute atoms and hence enriching the melt. The liquidus is assumed to be a straight line of slope  $m_e$ .

Before reaching steady-state, solute piles up in front of the advancing interface. The concentration of solute atoms in front of the

interface increases until the diffusion away from the interface equals the rate at which solute is rejected. The steady-state solute profile is shown in figure 1.4.



Expressed as a differential equation, this condition is:

$$D \frac{d^2C}{dz'^2} = 0 \quad (1.2)$$

in the primed coordinate system, and

$$D \frac{d^2C}{dz^2} + V \frac{dC}{dz} = 0 \quad (1.3)$$

in the unprimed coordinate system, where  $D$  is the diffusion coefficient for solute in the liquid and  $C$  is the spatially dependent concentration. Solving equation 1.3 with appropriate boundary conditions and then transforming into coordinates that move with the interface yields

$$C_L(z') = C_\infty \left[ 1 + \frac{1 - k_e}{k_e} \exp\left(\frac{-V}{D} z'\right) \right], \quad (1.4)$$

where  $C_L(z')$  is the concentration of solute in the liquid a distance  $z'$  from the interface and  $C_\infty$  is the initial concentration of solute in the melt (called  $C_\infty$  because the concentration of solute in the melt infinitely far from the interface remains at the initial amount).

For solidification near equilibrium, the temperature of the liquid adjacent to the interface  $T_\phi$  equals the equilibrium liquidus temperature  $T_{\text{liquidus}}$  for the composition of the melt at the interface. Using figure 1.3 as the equilibrium phase diagram, the liquidus temperature as a function of solute concentration is

$$T_{\text{liquidus}} = T_M + m_e C, \quad (1.5)$$

where  $T_M$  is the melting temperature of pure solvent, and  $m_e$  is the slope of the liquidus. Therefore, the temperature of the liquid at the interface is

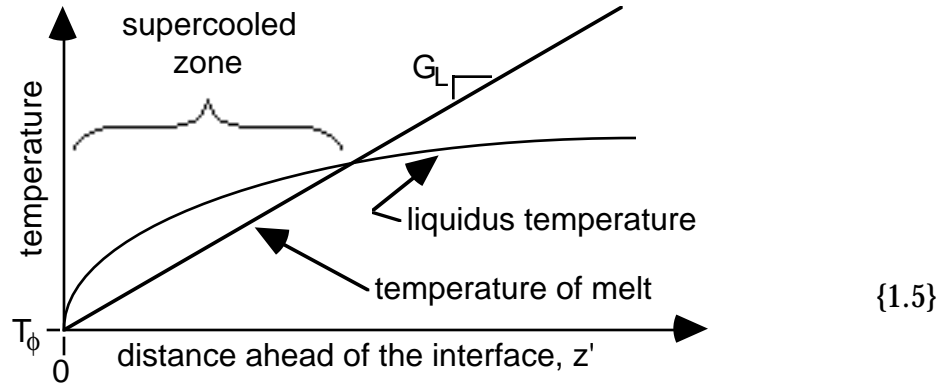
$$T_\phi = T_M + m_e C(z'=0^+). \quad (1.6)$$

The actual temperature of the melt at a distance  $z'$  from the interface is

determined by the temperature of the interface and the thermal gradient applied to the liquid  $G_L$

$$T(z') = T_\phi + G_L z' = T_M + m_e \frac{C_\infty}{k_e} + G_L z'. \quad (1.7)$$

The liquid layer at  $z'$  will be undercooled if  $T < T_\phi$ . Figure 1.5 shows equation 1.7 plotted over the temperature profile of figure 1.2.



Winegard and Chalmers [Winegard and Chalmers] point out that the existence of a supercooled liquid adjacent to the interface does not automatically imply that the interface will break down. For a protrusion to grow faster than the interface, the supercooling must also increase with distance into the melt. Expressed quantitatively, the Winegard-Chalmers condition for interface breakdown is

$$\left. \frac{d}{dz} [T_{\text{liquidus}}(z) - T(z)] \right|_{\phi} > 0 \quad (1.8)$$

where the derivative is evaluated at the interface ( $z' = 0$ ). When the two sides of this expression are equal, the system is at a point of marginal or neutral stability.

Expressing equation 1.8 in quantities other than temperature leads to the constitutional supercooling criterion for interface stability. Using equation 1.5 for the liquidus temperature and assuming a constant temperature gradient in the liquid ( $G_L = dT/dz$ ), the constitutional supercooling criterion is

$$\frac{G_L}{V} = - \frac{m_e C_\infty}{D} \left( \frac{1 - k_e}{k_e} \right). \quad (1.9)$$

This predicts any interface is stable at sufficiently low velocity, but eventually

becomes unstable as velocity increases. Equation 1.9 can be simplified by identifying the concentration gradient of the solute in the liquid adjacent to the interface (evaluate  $dC/dz'$  at  $z'=0$  from equation 1.3),

$$G_C = -\frac{V}{D} C_\infty \left( \frac{1-k_e}{k_e} \right). \quad (1.10)$$

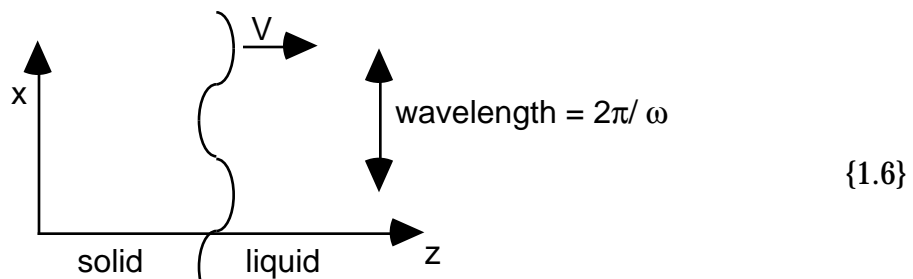
Now the constitutional supercooling criteria can be expressed as

$$G_L = m_e G_C. \quad (1.11)$$

Constitutional supercooling remains a powerful theory for solidification near equilibrium [Morris and Winegard, 1969; Tiller 1984], but its success in explaining experiments does not make up for its uncertain theoretical footing. The criterion for interface breakdown comes from considering the effect on the protrusion of undercooling away from the interface without considering how the protrusion would change the undercooling. As a minimum, the Gibbs-Thomson effect should lower the melting point at the tip of the protrusion so that the tip would see less undercooling.

### 1.1.3 Linear Stability Theory (perturbations, capillarity stabilization)

Mullins and Sekerka [Mullins and Sekerka, 1964] test interface stability by analyzing the growth or decay of infinitesimal perturbations on a planar interface. The picture is that of figure 1.6.



They develop the theory for a single Fourier component

$$\phi(x,t) = \delta(t) \sin(\omega x), \quad (1.12)$$

of spatial frequency  $\omega$  and infinitesimal amplitude  $\delta$ , then check stability for all values of  $\omega$ . The stability criterion is that an interface is unstable if the amplitude of any Fourier component grows with time ( $d\delta/dt$  having the same sign as  $\delta$ ). Note that the  $x$  coordinate is in the plane of the unperturbed interface. This opens a dimension that does not exist in the constitutional

supercooling analysis. As before, the system is in steady-state, and solid and liquid are in equilibrium with each other at each point on the interface. Figures 1.2 through 1.4 still apply.

Additional spatial variables change the equation for solute diffusion in the liquid to

$$\nabla^2 C + (V/D) (dC/dz) = 0 \quad (1.13)$$

(diffusion in the solid is still considered negligible). Modeling the effect of the perturbation on the thermal field requires the following equations for thermal diffusion:

$$\nabla^2 T_L + (V/A_L) (dT_L/dz) = 0 \quad (1.14a)$$

$$\nabla^2 T_S + (V/A_S) (dT_S/dz) = 0 \quad (1.14b)$$

where  $A_L$  and  $A_S$  are the thermal diffusivities of the liquid and solid. Equation 1.14a is for the liquid, 1.14b for the solid. Equations 1.13 and 1.14 are coupled by requiring both to give the same result for local interface velocity. Solidifying a certain volume of solid releases excess solute into the liquid and latent heat into the solid. The coupling of equations 1.13 and 1.14 assures that the solute field remove excess solute at the same rate as the thermal field removes the latent heat.

The boundary condition infinitely far from the interface is that the effect of the perturbations should die away. The boundary condition at the interface is that the interface must be in local equilibrium. The interface temperature is then

$$T_\phi = T_M + m_e C_\phi + T_M \Gamma \delta \omega^2 \sin(\omega x) \quad (1.15)$$

where  $T_M$  is the melting temperature of pure solvent when the interface is flat,  $C_\phi$  is the concentration of solute in the liquid at the interface,  $\Gamma$  is the capillarity constant (surface tension divided by latent heat), and  $\delta \omega^2 \sin(\omega x)$  is the interface curvature (calculated from equation 1.12). Equation 1.15 is just equation 1.6 with a term due to the Gibbs-Thomson effect.

Mullins and Sekerka linearize the interface response. The effect of the perturbation is to change the temperature and solute concentration at the interface by an amount proportional to the amplitude of the perturbation. Then the solutions to equations 1.13 and 1.14 are

$$T_\phi = T_0 + a\phi \quad (1.16a)$$

and

$$C\phi = C_0 + b\phi \quad (1.16b)$$

where  $T_0$  and  $C_0$  are values for the flat interface,  $a$  and  $b$  are expansion coefficients (to be determined), and  $\phi = \phi(x,t)$  is the amplitude of the perturbation. To simplify the math, Mullins and Sekerka also assume  $V/(A_L\omega) \ll 1$  and  $V/(A_S\omega) \ll 1$ . This assumption is good for our experiments. For  $\omega=100\text{nm}$ , and using the thermophysical properties of table 2.1 and Appendix B, we verify that

$$\frac{V}{A\omega} = \frac{1\text{m/s}}{(0.1\text{cm}^2/\text{s})(2\pi/100\text{nm})} = 0.0016 \ll 1 \quad (1.17)$$

which is a good approximation.

The central result is an expression for the amplification rate  $(d\delta/dt)/\delta$ :

$$\frac{d\delta/dt}{\delta} = \frac{V\omega\{...\}}{m_e G_C \omega + \frac{K_S G_S - K_L G_L}{K_S + K_L} \left[ \omega_C - \frac{V}{D}(1-k_e) \right]} \quad (1.18)$$

where the term in braces is

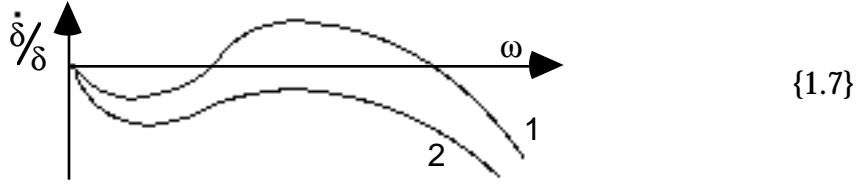
$$\begin{aligned} \{...\} = & -T_M \Gamma \omega^2 \left[ \omega_C - \frac{V}{D}(1-k_e) \right] \\ & - \frac{K_S G_S + K_L G_L}{K_S + K_L} \left[ \omega_C - \frac{V}{D}(1-k_e) \right] \\ & + m_e G_C \left[ \omega_C - \frac{V}{D} \right]. \end{aligned} \quad (1.19)$$

The new variables are

$$\omega_C = \frac{V}{2D} + \left[ \left( \frac{V}{2D} \right)^2 + \omega^2 \right]^{1/2}; \quad (1.20)$$

$G_L$  and  $G_S$  are temperature gradients at the unperturbed interface;  $K_L$  and  $K_S$  are the thermal conductivities of liquid and solid; and  $G_C$  is the concentration gradient at the unperturbed interface.

Figure 1.7 shows a plot of equation 1.18. If  $(d\delta/dt)/\delta$  is positive for any value of  $\omega$ , then the interface is unstable. For example, curve 1 in figure 1.7 represents an unstable interface because moderate wavelength perturbations will be amplified. Curve 2 represents a stable interface because all perturbations are damped.



The terms written out in equation 1.18 are always positive (if heat is flowing out of the system through the solid, then  $K_S G_S > K_L G_L$ ). Therefore the qualitative features of the equation can be deduced from equation 1.19. The first term accounts for capillarity; it goes to zero as the surface tension goes to zero. It is always negative because any perturbation will increase the area of the interface. The second term of equation 1.19 accounts for thermal diffusion. This term always acts to stabilize the interface. The third term accounts for solute effects. It is always positive, so it always acts against interface stability. Note that the capillarity term goes as  $\omega^2$ . Therefore capillarity damps short wavelengths (wavelength equals  $2\pi/\omega$ ) more strongly than long wavelengths. For sufficiently short wavelengths, the factor of  $\omega^2$  pushes  $(d\delta/dt)/\delta$  negative as shown in figure 1.7.

At this point we can make a qualitative comparison between the Mullins-Sekerka result and constitutional supercooling. The second and third terms of equation 1.19 show the same competition that was at the heart of the constitutional supercooling: thermal effects working for stability and solute effects working against. When

$$\frac{k_e T_M \Gamma V^2}{m_e G_C D^2} \ll 1 \quad (1.21)$$

capillarity can be neglected. Then the interface is stable when

$$m_e G_C < \frac{K_S G_S + K_L G_L}{K_S + K_L}. \quad (1.22)$$

This resembles equation 1.11 except that the thermal gradient is a weighted average of solid and liquid thermal gradients. Neutral stability in this approximation occurs when the two sides of equation 1.22 are equal. Expanding  $G_C$  and solving for  $C$  yields

$$C = \frac{m_e D}{V} \left( \frac{k_e}{k_e - 1} \right) \frac{K_S G_S + K_L G_L}{K_S + K_L}. \quad (1.23)$$

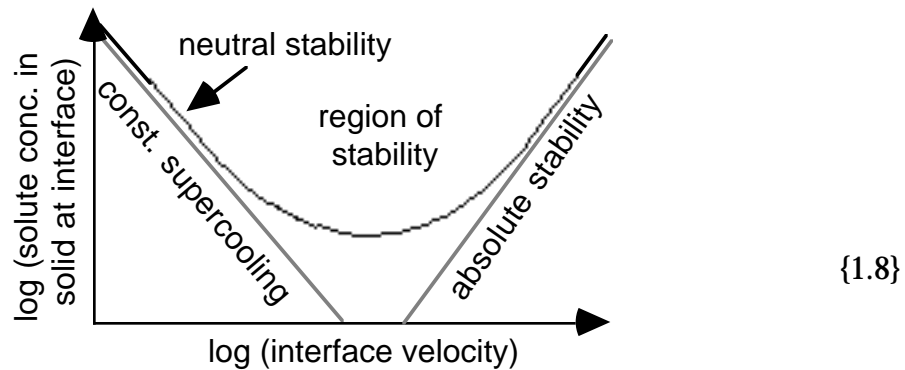
Equation 1.23 is the constitutional supercooling asymptote of the neutral stability curve.

At sufficiently high velocity, capillarity alone (the first term of equation 1.19) stabilizes the interface against the effects of excess solute (the third term of equation 1.19). The algebra is more complicated, but one arrives at a high velocity asymptote for the neutral stability condition:

$$C = \frac{k_e^2 T_M \Gamma V}{(k_e - 1) m_e D}. \quad (1.24)$$

The appearance of the various factors is logical. For example, a high value for the capillarity constant causes capillary effects to appear at lower velocity. A high velocity or low diffusion constant means that the characteristic diffusion length is small. Therefore only small wavelength perturbations can form, and these are the ones that capillarity damps the most. This limit is called absolute stability. It predicts that any interface is stable at sufficiently high velocity.

A neutral stability curve in  $(C_\infty, V)$  space looks something like figure 1.8. The asymptote with negative slope is the constitutional supercooling limit (equation 1.23); the asymptote with positive slope is the absolute stability limit (equation 1.24).



Actually calculating the neutral stability curve is difficult enough that Mullins and Sekerka leave explicit evaluation for a later paper [Sekerka, 1967]. One must find all sets of parameters such that the planar interface is unstable against no Fourier components, stable against most Fourier components ( $(d\delta/dt)/\delta < 0$ ), but marginally stable ( $(d\delta/dt)/\delta = 0$ ) with respect to at least one Fourier component of non-zero frequency. Equation 1.18 is cubic in  $\omega$  with one root fixed at zero. The other two roots must exist as a double root. (Solving numerically for neutral stability is a good test for root finding routines!)

An excellent review article by Trivedi and Kurz [Trivedi and Kurz, 1986] includes a version of the Mullins-Sekerka analysis with fewer restrictions. To apply the theory to the dendrite problem, they drop the assumption that  $V/(A_L\omega) \ll 1$  and  $V/(A_S\omega) \ll 1$ . They also show how to take into account diffusion in the solid. Diffusion in the solid stabilizes the planar interface, but the effect is small —proportional to the ratio of solute diffusivity in the solid to solute diffusivity in the liquid. For tin in silicon at 1685K, the ratio is  $2e-11/2.5e-4$  [Mayer and Lau, 1972], so the effect is negligible.

## 1.2 Nonequilibrium Solidification Theory

The striking result of the Mullins-Sekerka stability analysis compared to the constitutional supercooling analysis is the absolute stability limit. For any solute concentration, the interface is stable at sufficiently high velocity because of capillarity. The theory is well-tested. For example, in dilute silver-copper alloys, Boettinger, Shechtman, Schaefer, and Biancaniello [Boettinger *et al.* 1984] observe growth of solid solutions at velocities that compare favorably with the predictions of equation 1.24. For higher concentration alloys, the absolute stability velocity is higher, and agreement with theory degenerates. Rapid solidification experiments by White *et al.* [White *et al.* 1980] have shown that for several silicon alloys there is stability at high velocities where the simple constitutional supercooling criterion would have predicted an unstable interface. Like the results for silver-copper however, the theory breaks down at such high solidification velocities.

If the interface moves rapidly enough, it does not have time to equilibrate with the liquid it overtakes. Baker and Cahn's measurements in the zinc-cadmium system [Baker and Cahn, 1969] demonstrate that this regime is experimentally observable. They chose the zinc-cadmium system because the equilibrium solidus for cadmium dissolved in zinc is retrograde. The maximum solubility occurs at a temperature above the eutectic. By solidifying a supersaturated solution in a retrograde system, Baker and Cahn showed that the mechanism could not be as simple as a metastable extension of the equilibrium solidus or suppression of a competing equilibrium phase. Their cadmium-zinc alloy could have been formed only under nonequilibrium conditions.

### 1.2.1 Solute Trapping

Baker and Cahn [Baker and Cahn, 1969] introduce the notion of solute trapping for cases where the chemical potential of the solute rises upon going from liquid to solid (a true nonequilibrium process). They also show that for systems with a retrograde solidus such as zinc-cadmium or silicon-tin, suppressed partitioning implies solute trapping. Therefore, the terms can be used interchangeably for silicon-tin. Solute trapping is quantified using a nonequilibrium partition coefficient,  $k$  (no subscript). White, Wilson, Appleton, and Young [White *et al.* 1980] and Baeri, Poate, Campisano, Foti, Rimini, and Cullis [Baeri *et al.* 1980] report many values of  $k$  that exceed  $k_e$ .

The continuous growth model of Aziz and Kaplan [Aziz and Kaplan, 1988] successfully fit the data for silicon alloys [Aziz *et al.* 1986] and subsequent data for aluminum alloys [Smith and Aziz, 1994]. In the dilute limit, their equation for the partition coefficient as a function of velocity is

$$k(v) = \frac{k_e + (v/v_D)}{1 + (v/v_D)} \quad (1.25)$$

where the diffusive velocity  $v_D$  is a fitting parameter (see [Smith and Aziz, 1994] for theory about  $v_D$ ). Note that  $k$  approaches  $k_e$  as velocity approaches zero and that  $k$  approaches unity as velocity becomes large.

### 1.2.2 Interfacial Undercooling

Baker and Cahn [Baker and Cahn, 1971] point out that a complete theory of nonequilibrium solidification has four equations. The first pair, equations 1.12 and 1.13, describe the transport of latent heat and excess solute away from the interface. The second pair describe what happens at the interface:

$$C(\text{solid}) = f(V, C_\phi), \quad (1.26a)$$

solute concentration in the solid as a function of velocity and solute concentration in the liquid at the interface, and

$$T_\phi = f(V, C_\phi) \quad (1.26b)$$

interface temperature as a function of interface velocity and solute concentration in the liquid at the interface. Equation 1.26a has already been introduced in equations 1.1 (definition of  $k$ ) and 1.25 (continuous growth model). Equation 26b is given below as equations 1.29-1.31.

Boettinger, Coriell, and Trivedi [Boettinger *et al.* 1988] derive an analytical expression for the interface response functions that constrain the parameters to vary in a thermodynamically consistent way. Starting with Baker and Cahn's expression [Baker and Cahn, 1971] for the driving force  $\Delta G$  per mole for solidification of a Henrian solution, they assume straight-line equilibrium liquidus and solidus (figure 1.3) and obtain

$$\frac{\Delta G}{RT_\phi} = \frac{-L_M}{RT_M^2} (T_M + m_e C_\phi - T_\phi) + C_\phi \left[ k_e - k \left( 1 - \ln \frac{k}{k_e} \right) \right] \quad (1.27)$$

where  $R$  is the gas constant and  $L_M$  is the heat of fusion per mole at the melting point. They eliminate  $\Delta G$  by assuming simple linear kinetics:

$$V = V_0 \left[ 1 - \exp\left(\frac{\Delta G}{RT_\phi}\right) \right] \approx -V_0 \left(\frac{\Delta G}{RT_\phi}\right) \quad (1.28)$$

The parameter  $V_0$  is the interface velocity at maximum driving force (the speed with which atoms in the liquid can move onto lattice sites in the solid; it can be as high as the speed of sound). Eliminating  $\Delta G$  and isolating  $T_\phi$  yields the second interface response function,

$$T_\phi = T_M + \tilde{m} C_\phi - \mu V, \quad (1.29)$$

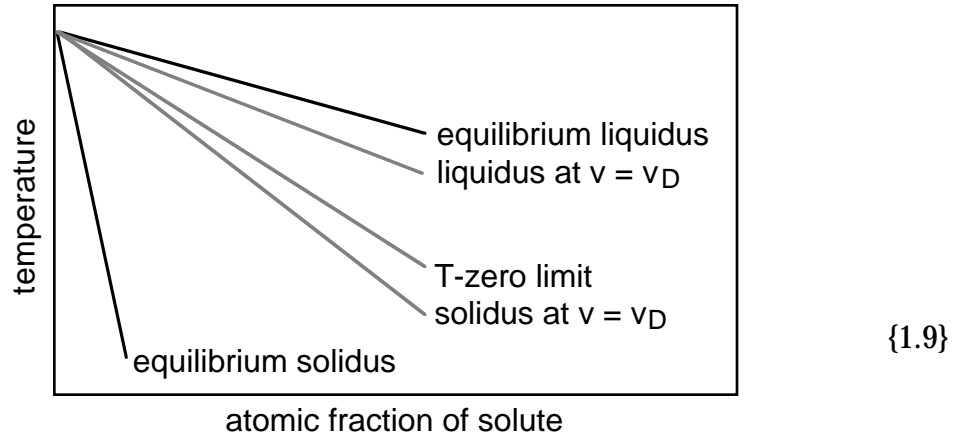
where

$$\frac{1}{\mu} = \frac{RT_M^2}{L_M} \left(\frac{V}{V_0}\right) \quad (1.30)$$

describes the effect of finite attachment kinetics and

$$\tilde{m} = m_e \left\{ 1 + \frac{k_e - k \left[ 1 - \ln(k/k_e) \right]}{1 - k_e} \right\} \quad (1.31)$$

describes the kinetic liquidus. Figure 1.3 (the equilibrium phase diagram) along with equations 1.25 (solute trapping) and 1.29 (interfacial undercooling) describe the nonequilibrium phase diagram in the dilute solution regime. Figure 1-9 shows the results for a velocity near zero (the equilibrium phase diagram), a velocity equal to the diffusive velocity (substantial deviations from equilibrium), and the T-zero limit. (Beyond the T-zero limit, the liquid has lower free energy than the solid, so solidification is impossible. To calculate the T-zero curve from equation 1.27, set  $\Delta G$  to zero and  $k$  to one, then solve for  $T_\phi$  as a function of  $C_\phi$ .)



As in figure 1.3, figure 1.9 shows  $k_e$  much less than unity. Note that solute trapping causes the solidus to move towards the T-zero limit much sooner than the liquidus. The liquidus will not be so close to the T-zero limit until the velocity is several times the diffusive velocity.

## 1.3 Nonequilibrium Stability Theory

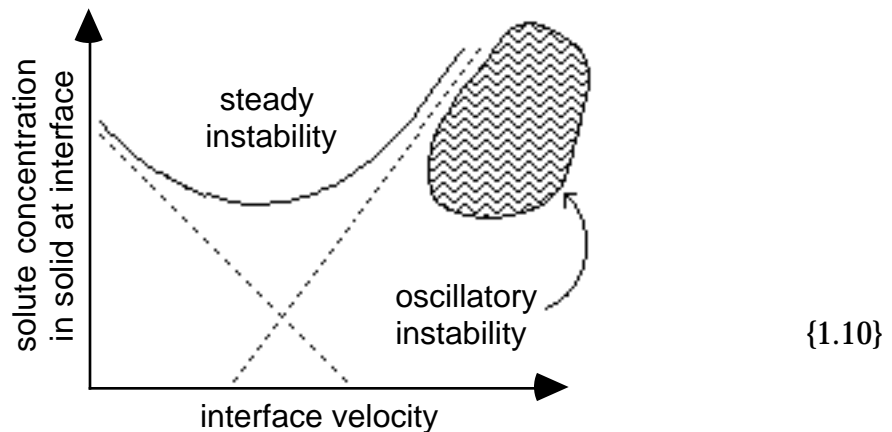
### 1.3.1 Background

Coriell and Sekerka [Coriell and Sekerka, 1983] were the first to integrate nonequilibrium effects into stability theory. The interrelationships between  $k$ ,  $C$ , and  $T$  are important enough that simply substituting  $k(v)$  for  $k_e$  does not provide a complete picture. They use a perturbation of the form

$$z' = w(x,y,t) = \delta \exp[\sigma t + i(\omega_x x + \omega_y y)] \quad (1.32)$$

(where  $\delta$  and the  $\omega$ 's are real and  $\sigma$  is complex; the physical amplitude of the perturbation is the real part of  $w$ ). The time dependence is explicit in the variable  $t$ . The interface is stable if the real part of  $\sigma$  is negative for all  $\omega$ 's. The interface is unstable if the real part of  $\sigma$  is positive for some  $\omega$ . There are two kinds of instability. If  $\sigma$  is purely real, the perturbations evolve steadily (monotonically increasing) as in the equilibrium stability problem. If  $\sigma$  has an imaginary part, the perturbations oscillate. An oscillatory instability changes cyclically between being a protrusion and a trough, but the amplitude of the oscillation increases with time. This new instability mode is located in the

vicinity of the shaded area of figure 1.10.



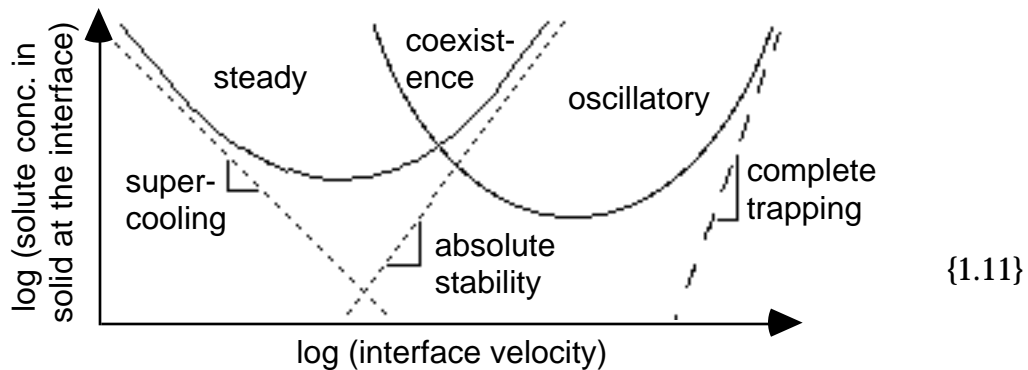
Like a steady instability, an oscillatory instability grows because there is a mechanism that maintains an uneven distribution of solute. For steady instabilities, the mechanism is lateral diffusion of solute. For oscillatory instabilities, the mechanism is the solute pump. Mathematically, the solute pump arises from the derivative of the partition coefficient with respect to velocity. Physically, the solute pump is a variation in local velocity along the interface which causes a variation in partitioning. A protrusion racing ahead of the interface traps solute until the local liquidus temperature exceeds the local temperature. In the mean time, the slow section of the interface has rejected enough solute into the trough to cause local constitutional supercooling. This section of interface now races forward and passes the former protrusion. As the velocity increases, so does trapping; solute rejection at the tip of the protrusion increases until the supercooling disappears. The former trough has become a protrusion that cannot maintain its velocity. In the mean time, reject of solute from the sides of the new protrusion have accumulated in the new trough. The former tip has become a trough full of supercooled liquid. One half cycle has elapsed. In general, if a sinusoidal variation in velocity is ninety degrees out of phase with a sinusoidal variation in interface position, the perturbation will grow.

Why can the interface be unstable past the absolute stability limit? The distribution of solute along the interface is determined by the distribution of local velocity along the interface. Therefore, the wavelength of the perturbation is independent of interface curvature and is unaffected by the capillarity. The wavelength can be quite long even at high velocity. Oscillatory

instabilities do not exist at low velocities because the rate change of partitioning with velocity ( $dk/dV$ ) is too small. There are two limits on the high velocity side. First,  $dk/dV$  becomes small again as  $k$  approaches unity. Second, finite attachment kinetics ( $V_0$  in equation 1.29) slow down the interface process thereby suppressing rapid oscillations in velocity. Colloquially, the difficulty that atoms have attaching to solid-liquid interface (for example, silicon atoms getting their bonds oriented correctly) make the interface kinetics too “sluggish” for oscillatory instabilities.

### 1.3.2 Work of Davis and coworkers

Merchant and Davis [Merchant and Davis, 1990] and Huntley and Davis [Huntley and Davis, 1993a] incorporate the dilute form of the continuous growth model for partitioning (equation 1.25) and the kinetic liquidus constraint on interface temperature (equation 1.29) into linear stability theory and obtained a full numerical solution for the time-independent characteristic equation (the non-equilibrium equivalent of equations 1.18 through 1.20). For perturbations of the form of equation 1.32, neutral stability against steady instabilities occurs when both the real and imaginary parts of  $\sigma$  are zero. Neutral stability against oscillatory instabilities occurs when the real part of  $\sigma$  is zero and the imaginary part is non-zero. In general, the result looks something like figure 1.11.



The full solution presents a variety of instabilities (the silicon-tin system is much simpler). For example, one oscillatory mode has wave number zero which implies a banded microstructure. The solute concentration on any plane parallel to the interface is constant, but the concentration varies along the direction of solidification. There also exists a

region where steady and oscillatory instabilities coexist. Possibilities such as these may be related to the banded microstructures observed several metallic alloy systems [see Carrard *et al.* 1992]. Another new feature is the window of stability. Under certain conditions, the interface is stable for a range of velocities bounded on one side by oscillatory instabilities and on the other by steady instabilities. Boettinger, Shechtman, Schaefer, and Biancaniello [Boettinger *et al.* 1984] also report this kind of behavior.

Figure 1.12 is the neutral stability curve that Huntley and Davis [Huntley and Davis, 1993a] calculate for silicon-tin (using parameters comparable to those in table 2.1). The region of oscillatory instability lies entirely within the region of steady instabilities; the interface is so sluggish that the region of instability against oscillatory instabilities lies entirely within the region of instability against steady instabilities. Therefore the limit of interface stability is the neutral stability curve against steady perturbations. The calculation turns out to be only slightly harder than in the equilibrium case because the time-dependence that is so important for calculating oscillatory instabilities no longer matters. The neutral stability curve against steady instabilities is exactly equation 1.29 set equal to zero with equation 1.25 and 1.31 substituting for the equilibrium liquidus and equilibrium partition coefficient. This the method of calculation for the results shown in chapter 5.

Figure 1.11  
Neutral stability curve for Merchant-Huntley-Davis analysis

Thanks to D.A. Huntley for calculating and plotting the data.  
Used with permission.



Karma and Sarkissian [Karma and Sarkissian, 1993] have another formulation but do not give calculations for silicon-tin. They use the same version of solidification theory, but analyze interface stability using a Green's function solution to the time-dependent equations. For steady instabilities, their method gives identical results to that of Huntley and Davis [Huntley and Davis, 1993b]. It has certain advantages suitable for studying oscillatory instabilities, but for a sluggish interface like silicon-tin, the results should be identical to those of Huntley and Davis.

### 1.3.3 Work of Brunco

Coriell and Sekerka [Coriell and Sekerka, 1983] analyze the effects of a perturbation by expanding about the solution for the planar interface. An advantage of partial derivative expansions is that one is not restricted to a straight line equilibrium phase diagram. The phase diagram need only be differentiable, making it possible to extend the results to non-dilute solutions. Also, in 1983 any nonequilibrium theory had to be general. There was little quantitative data on nonequilibrium solidification, and there was no complete model in the literature. The gap in knowledge had two effects. First, the deviations from equilibrium are not constrained to be thermodynamically consistent (Coriell and Sekerka expect the constraint to be part of the model for solidification; this is indeed true for the model of section 1.2). Second, Coriell and Sekerka cannot evaluate any of the partial derivatives that appear in the expansions.

Even with the model of section 1.2, it is hard to do the calculations for Coriell and Sekerka's theory. The required partial derivatives are too awkward. Merchant and Davis found it easier to work the constraints into the governing equations, then apply stability theory in the Mullins-Sekerka way. Brunco [Brunco, 1995] comes closer to following Coriell and Sekerka's lead. By starting slightly differently and doing the partial derivative expansions differently, he obtains a stability theory that can then be evaluated using the model of section 1.2. Along the way, he introduces a novel method for including interface curvature into the equations for solidification.

Brunco [Brunco, 1995] starts with a solidification velocity proportional to the driving force (equation 1.28; Brunco equations 5.10 and

5.11). The energy divides into two components,

$$\Delta G = \Delta G_f + \Delta G_\omega. \quad (1.33)$$

where  $\Delta G_f$  is the change in free energy due to solidification and  $\Delta G_\omega$  is the free energy due to the curvature of the interface. Dividing the free energies also divides the contributions to velocity into solidification and curvature components:

$$V = v_f + v_\omega = -V_0 \frac{\Delta G_f}{RT} - V_0 \frac{\Delta G_\omega}{RT} \quad (1.34)$$

discussed in turn below.

The contribution to velocity from solidification is in terms of the change in chemical potential when solute and solvent atoms change from liquid to solid. If the interface always remained planar,  $V$  would be exactly  $v_f$ . The effect of the perturbation expressed as a partial derivative expansion about the velocity of the planar interface is:

$$v_f = V + \mu_T b \phi + \mu_X a \phi \quad (1.35)$$

where  $\mu_T$  is the partial derivative of  $v_f$  with respect to temperature at constant concentration, and  $\mu_X$  is the partial derivative of  $v_f$  with respect to concentration at constant temperature,  $a$  and  $b$  are the strength of the interface response (as in equation 1.16), and  $\phi$  is the amplitude of the perturbation.

The contribution to velocity due to free energy tied up locally in a curved interface is proportional to the interfacial energy and the interfacial curvature. The curvature calculated from equation 1.32 is  $\omega^2 \phi$ . Assuming that the surface energy is constant, the partial derivatives are zero, so the only term in the expansion is the nominal value:

$$v_\omega = -V_0 \frac{\Delta G_\omega}{RT} = -\mu_T^0 \Gamma \omega^2 \phi \quad (1.36)$$

where

$$\mu_T^0 = -\frac{V_0 L_M}{RT^2}. \quad (1.37)$$

The latent heat appears only as a consequence of the definition of  $\Gamma$ . Equation 1.36 produces a component of velocity that is negative where the interface protrudes, thus tending to flatten the interface.

The rest of the analysis follows the method of Coriell and Sekerka: solve time-dependent partial differential equations for heat flow and

solute diffusion, impose an infinitesimal perturbation (equation 1.32), linearize the interface response (equations like 1.35), apply boundary conditions, and solve for perturbation growth rate (Brunco equation 5.44). Setting the growth rate to zero gives the neutral stability curve.

The partial derivatives could be evaluated using the solidification model of section 1.2. The disadvantage of using those equations is that they all assume a dilute solution. Brunco's formulation is more general. He takes the forms of the equations for solute trapping (equation 1.25) and driving force for solidification (equation 1.29) suitable for Henrian solutions [Aziz and Kaplan, 1988; Baker and Cahn, 1971] and obtains an interface stability theory for solidification of Henrian solutions. For silicon-tin though, the dilute solution approximation is adequate. Figure 1.13 shows Brunco's results for silicon-tin.

Figure 1.13

Neutral stability curve for silicon-tin calculated by Brunco

Thanks to D.P. Brunco for calculating and plotting the data.

Used with permission.



## 1.4 Previous Experiments

Experimental tests of interface stability predate pulsed laser melting. Morris and Winegard [Morris and Winegard, 1969] make a detailed test of constitutional supercooling theory in the cm/sec velocity regime. They find detailed agreement between the prediction of the limit of interface stability and the transition from solid solution to cellular morphology. The literature also contains many tests of the Mullins-Sekerka theory such as the experiments with silver-copper alloys mentioned above [Boettinger *et al.* 1984]. Partly because of a high equilibrium partition coefficient ( $k_e=0.45$ ), dilute silver-copper alloys reach absolute stability before nonequilibrium effects become noticeable. Therefore, the experiment is a useful test of the local-equilibrium theory. Although Boettinger *et al.* find good agreement between theory and experiment at low velocity, as the velocity (and concentration) of the experiments increase, the agreement deteriorates. Theories that assume local equilibrium cannot accurately predict what happens far from equilibrium.

The literature contains several investigations of interface stability during rapid solidification [Cullis *et al.* 1981; Narayan, 1982; Campisano and Poate, 1985]. The work of Campisano and Poate is typical. They use pulsed laser melting to make supersaturated solid solutions of silicon-indium and silicon-bismuth. They obtain solid solutions in regions of velocity-concentration space where the equilibrium theory predicts the interface is unstable. However, the result does not constitute a quantitative test of the stability theory. The first problem is incomplete theory. They compare their data with Sekerka's [Sekerka, 1967] asymptotic form of the absolute stability limit (equation 1.24), except that they substituted the nonequilibrium partition coefficient for the equilibrium one. This modification to the Mullins-Sekerka theory ignores the thermodynamic constraints of equations 1.29 to 1.31 [Boettinger *et al.* 1988]. The second problem is that they did not make direct measurements of velocity, so their velocities and partition coefficients are estimates. These estimates are based on heat flow simulations, but the value of thermal conductivity of amorphous silicon used in the simulation was too

high. Any agreement with experiment is fortuitous. Therefore, their result can only be considered as qualitative evidence that nonequilibrium effects stabilize the interface.

A good understanding of solute trapping is essential to a quantitative test. The deviations from equilibrium become noticeable in the range of velocities where the neutral stability curve (approximated by equation 1.24) goes as  $k^2/(1-k)$ . In this range, even a small amount of solute trapping significantly changes the critical concentration for breakdown. For example, increasing  $k$  from 0.02 to 0.03 more than doubles the critical concentration for breakdown. This is not surprising. In the theory, the instability is due to excess solute at the interface. Solute trapping stabilizes the interface by reducing the amount of solute rejected into the liquid. We will therefore base our study of interface stability on quantitative measurements of the partition coefficient.

Although the search for the limit of interface stability is a search for the maximum substitutional concentration, a search for the maximum substitutional concentration is not necessarily a test of interface stability. To understand this, we examine the literature on maximum substitutional concentration.

White, Wilson, Appleton, and Young [White *et al.* 1980] report on a broad investigation of limits to the maximum substitutional concentration of group III-V elements in silicon. Different mechanisms are at play in different alloy systems. For example, boron causes a unidirectional contraction of the silicon lattice. At sufficiently high concentration, that lattice fails under the stress and cracks open. For arsenic, incorporation is limited by thermodynamic considerations. Solidification takes place at the T-zero curve (shown in figure 1.9). At higher concentration, the liquid has lower free energy than the solid, so solidification is impossible. For tin and antimony, the limit is cellular breakdown. The data for tin constitute a test of linear stability theory, but like the result of Campisano and Poate [Campisano and Poate, 1985], the data are qualitative.

Several investigators [Lombardo *et al.* 1991; Kramer *et al.* 1992; Brunco, 1995] have discussed interface stability in the silicon-germanium

system. Strain effects make the system undesirable for doing quantitative measurements, but the qualitative results highlight another subtlety in the relationship between interface stability and maximum substitutional concentration. In this system, the maximum substitutional concentration is unity because the two components are perfectly miscible. However, pulsed laser melting experiments have never made a defect-free solid solution with a germanium concentration higher than about 21%. The finite width of the two phase region (the phase rule again) means that the solid will reject solute into the melt. The excess solute then makes the interface unstable. Therefore, if the solubility limit is not set by strain, it is set kinetically by interface stability even though there is no thermodynamic limit.

Table 1.1

Symbols and definitions for stability theory

a	expansion coefficient in equation 1.16a (intermediate variable)
$A_L$	thermal diffusivity of the liquid
$A_S$	thermal diffusivity of the solid
b	expansion coefficient in equation 1.16b (intermediate variable)
C	concentration (generic)
$C_0$	concentration when the interface is flat
$C_L$	solute concentration in liquid ( $C$ for $z' > 0$ )
$C_\infty$	solute concentration in melt infinitely far from interface
$C_\phi$	solute concentration in liquid adjacent to interface
D	diffusivity of solute in liquid solvent
$G_C$	solute gradient in the liquid at the interface
$G_L$	temperature gradient in liquid
$G_S$	temperature gradient in solid
k	partition coefficient
$k_e$	equilibrium partition coefficient
$K_L$	thermal conductivity of liquid
$K_S$	thermal conductivity of solid
$L_M$	heat of fusion per mole at the melting point
$m_e$	equilibrium liquidus slope
$\tilde{m}$	kinetic liquidus slope

Table 1.1

R	gas constant
T	temperature (generic)
$T_L$	temperature in the liquid (T for $z' > 0$ )
$T_S$	temperature in the solid (T for $z' < 0$ )
$T_\phi$	the temperature at the interface (boundary condition is $T_L = T_S = T_\phi$ )
$T_M$	melting temperature of the pure solvent
$T_{\text{liquidus}}$	liquidus temperature on equilibrium phase diagram
$T_0$	temperature for the flat interface taken in the liquid adjacent to the interface
V	velocity of planar interface
$V_0$	interface velocity at maximum driving force
$v_D$	diffusive velocity; disequilibrium parameter in $k(v)$
$v_f$	velocity component due to solidification
$v_\omega$	velocity component due to changing the curvature of the interface
z	direction of solidification
$z'$	coordinate system attached to interface
$\Gamma$	capillarity constant (surface tension divided by latent heat)
$\delta$	perturbation amplitude
$\sigma$	perturbation amplitude (a complex number)
$\omega$	spatial frequency of Fourier component of perturbation
$\omega_x$	spatial frequency of Fourier component along x axis
$\omega_y$	spatial frequency of Fourier component along y axis
$\omega_C$	intermediate variable
$\Delta G$	driving force per mole for solidification of a Henrian solution
$\Delta G_f$	change in free energy due to solidification
$\Delta G_\omega$	change in free energy due to changing the curvature of the interface
$\mu$	reciprocal interface sluggishness (related to attachment kinetics)
$\mu_T^0$	an intermediate result (equations 1.35-1.37)
$\mu_T$	partial derivative of $v_f$ with respect to temperature at constant concentration
$\mu_X$	partial derivative of $v_f$ with respect to concentration at constant temperature

# Chapter 2

## Experimental Methods

### 2.1 Choice of Alloy System

In principle, stability theory applies equally well to any binary alloy. The choice of silicon-tin is motivated largely by a single consideration: we can measure all the important input parameters. This thesis tests the combination of a particular stability theory and a particular model for nonequilibrium solidification. The test is quantitative, and there are no adjustable parameters. The usefulness of the test therefore hinges on having accurate values for the input parameters. For the velocity range of our experiments, the important parameters are those in the nonequilibrium form of equation 1.24, the absolute stability asymptote of the neutral stability curve

$$C = \frac{k^2 T_M \Gamma V}{(k-1) \tilde{m} D}. \quad (2.1)$$

The values come from the following sources.

Some parameters are well established, and have been in the literature for a long time. The melting point of pure solvent  $T_M$  is one of these [Hultgren *et al.* 1973]. Another is the latent heat (hidden in  $\Gamma$ ) [Hultgren *et al.* 1973]. The parameters for the equilibrium phase diagram in the dilute

solution regime (equilibrium partition coefficient and equilibrium liquidus slope) come from the phase diagram [Thurmond and Kowalchik, 1960].

Laser melting and solute trapping experiments give  $k(V)$  and  $D$ , and hence the rest of  $\tilde{m}$ . The techniques are well established; see section 3.1.2 for a discussion and references. The nonequilibrium partitioning parameters were not available in the literature at the start of this project. Thus, this measurement was our first step; see chapter 4 for the results. For this chapter, we simply note that although both solute trapping measurements and interface stability measurements use ion implantation and laser annealing, the sample design and data analysis are completely different. And although  $v_D$  is a fitting parameter in solute trapping experiments, once measured it cannot be adjusted in the stability experiment.

The other part of the capillarity constant  $\Gamma$  is the surface tension. We use the value found in homogeneous nucleation experiments [Evans and Stiffler, 1991]. There is some uncertainty because a nucleation experiment measures surface tension averaged over many orientations. In planar solidification experiments, the surface tension for (100) dominates the behavior. If the surface tension is anisotropic, there may be some difference, although by the time the perturbation amplitude is large enough to detect, the differences may average out. Also, there is no measure of the effect of tin on surface tension. If tin prefers to segregate to the interface, the surface tension would lower.

All of the calculation presented in chapter 5, as well as those of Huntley and Davis [Huntley and Davis, 1993a] and Brunco [Brunco, 1995], use the value measured by Evans and Stiffler. Recent results by Shao and Spaepen [Shao and Spaepen, 1995] indicate that the value for surface tension (at 1685K) is higher. We have also tried their number in our calculations. However, in the rapid solidification regime, the neutral stability curve is proportional to the surface tension, so the difference in surface tension looks small on log-log plots. See figure 6.1 for a comparison.

This covers all of the parameters of equation 2.1. Other parameters play a minor role. For the thermal conductivity of solid and liquid, we take the values recommended by Ho *et al.* [Ho *et al.* 1971]. The temperature

gradient in the solid is well approximated by the product of velocity and latent heat divided by the thermal conductivity of the solid. A typical value is

$$G_S = \frac{V L_M}{K_S} = \frac{1\text{m/s} \times 4.19 \times 10^9 \text{J/m}^3}{22\text{W}/(\text{K}\cdot\text{m})} = 1.9 \times 10^8 \text{ K/m.} \quad (2.2)$$

The thermal gradient in the liquid is estimated to be  $2 \times 10^4 \text{ K/m}$  using heat flow simulations (note  $G_L < G_S$ ). In the velocity range of this experiment however the predictions are highly insensitive to thermal parameters. Values for all parameters are given in table 2.1.

Table 2.1

Inputs to calculation of silicon-tin interface stability as plotted in chapter 5

$D = 2.5 \times 10^{-4} \text{ cm}^2/\text{s}$	diffusivity of tin in liquid silicon [Hoglund <i>et al.</i> 1991]
$v_D = 17 \text{ m/s}$	diffusive velocity [Hoglund <i>et al.</i> 1991]
$G_L = 20000 \text{ K/m}$	thermal gradient in the liquid (heat flow simulations)
$G_S$	thermal gradient in the solid (equation 2.2)
$K_L = 140 \text{ W}/(\text{K}\cdot\text{m})$	thermal conductivity of the liquid at melting point [Ho <i>et al.</i> 1971]
$K_S = 22 \text{ W}/(\text{K}\cdot\text{m})$	thermal conductivity of the solid at melting point [Ho <i>et al.</i> 1971]
$T_M = 1685 \text{ K}$	melting temperature of pure silicon [Hultgren <i>et al.</i> 1973]
$k_e = 0.016$	equilibrium partition coefficient [Thurmond and Kowalchik, 1960]
$m_e = -460 \text{ K}$	slope of equilibrium liquidus (van 't Hoff rule)
	$m_e = (1-k) \frac{RT_M^2}{L_M}$
$0.36 \text{ J/m}^2$	surface tension [Evans and Stiffler, 1990]
$0.45 \text{ J/m}^2$	surface tension [Shao and Spaepen, 1995]
$L_M = 4.19 \times 10^9 \text{ J/m}^3$	latent heat of fusion at melting temperature [Touloukian, 1970]

In addition to having values for all the important parameters, silicon-tin has practical advantages. Silicon alloys have been used extensively for pulsed laser melting experiments largely because high quality silicon is readily available and readily processed. Tin is a good solute for several reasons. On the phase diagram [Massalski, 1986], the room temperature solubility of tin in silicon is negligible. Therefore we can achieve high supersaturations while staying in the dilute solution regime. The solidus is retrograde with a maximum equilibrium solubility of 0.1 atomic percent at 1339K. As in Baker and Cahn's experiments with silver-copper, a supersaturated solid solution implies nonequilibrium solidification. Finally, tin is in the same column of the periodic table as silicon, but down two rows. The similarity in electron configuration means that tin does not dope silicon, and therefore will not interfere with conductance measurements. The difference in mass provides good contrast for scattering analysis.

## 2.2 Sample Preparation

All samples are made by ion implantation of tin into commercial silicon wafers (bulk resistivity of 8 to 200  $\Omega$ -cm). The wafers are of three types: bulk Si(100), bulk Si(111), and thin-film silicon-on-sapphire (SOS) with 0.5 $\mu$  Si(100) on (1 $\bar{1}$ 02) sapphire. The SOS samples are superior for making quantitative measurements of solidification velocities (see chapter 3) whereas the bulk samples are superior for measuring interface stability. When implanting tin, we use isotope  $^{120}\text{Sn}$ ; implant energies range from 40 to 165 keV, and doses range from  $10^{15}$  to  $10^{17}$  ions per square centimeter. We choose doses and energies so that the near surface region is amorphous. We also implant some wafers with a low dose of boron to create a marker layer (discussed at the end of section 3.2). Table 2.2 shows details for the implants.

Table 2.2

## Ion implantation recipes

label	tempe rature	$^{120}\text{Sn}$ implant		low energy $^{11}\text{B}$ implant		high energy $^{11}\text{B}$ implant	
		$\text{cm}^{-2}$	keV	$\text{cm}^{-2}$	keV	$\text{cm}^{-2}$	keV
SOS1	LN <sub>2</sub>	3e15	100				
SOS2	LN <sub>2</sub>	5e15	100				
SOS3	LN <sub>2</sub>	8e15	100				
SOS4	LN <sub>2</sub>	1e16	100				
SOS5	LN <sub>2</sub>	3e16	100				
SOS6	LN <sub>2</sub>	1e17	100				
SOS7	LN <sub>2</sub>	1e16	40				
IS01	room	2e16	165	3e15	100	5e15	200
IS02	room	1e16	165	3e15	100	5e15	200
IS03	room	5e15	165	3e15	100	5e15	200
IS04	room	3e15	165	3e15	100	5e15	200
IS05	room	1e16	165	5e15	100	8e15	200
IS06	room	1e16	165	2e15	100	8e15	200
IS07	room	1e16	165				
IS08	room	2e16	165	3e15	100	5e15	200
IS09	room	5e16	165	3e15	100	5e15	200
IS10	room	7e15	120	3e15	100	5e15	200
IS11	room	3.5e15	120	3e15	100	5e15	200
IS12	room	1.4e16	120	3e15	100	5e15	200
111Sn1	LN <sub>2</sub>	1e16	165				
111Sn2	LN <sub>2</sub>	2e16	165				
111Sn4	LN <sub>2</sub>	4e16	165				

We use the SOS samples for electrical conductance measurements. After implantation, they are patterned, etched, given aluminum contacts, and briefly annealed in a furnace. Before pulsed laser melting, wafers are cleaved or diced into individual samples (2.5 to 3 mm wide by 5 mm high). A clean sample surface is important. The samples are kept as clean as possible,

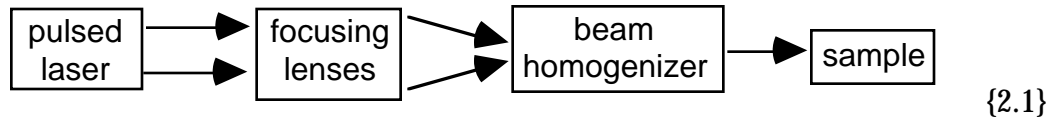
and we clean them in acetone, methanol, and distilled water before pulsed laser melting. The samples patterned for conductance measurements are delicate, but ultrasonic cleaning works well on the bulk silicon samples.

## 2.3 Experimental Setup

Rapid solidification is based on rapid melting using a pulsed laser. When the laser pulse is incident on the sample, the optical energy is absorbed near the surface and quickly converted to thermal energy. The laser pulse is so intense that energy is deposited faster than it diffuses into the bulk. The thermal gradient becomes very steep, but the surface still heats to melting. After tens of nanoseconds, the laser pulse ends, and the steep thermal gradient rapidly cools the liquid. The liquid cools at a rate of about a billion degrees a second causing the solid-liquid interface to move around one meter per second.

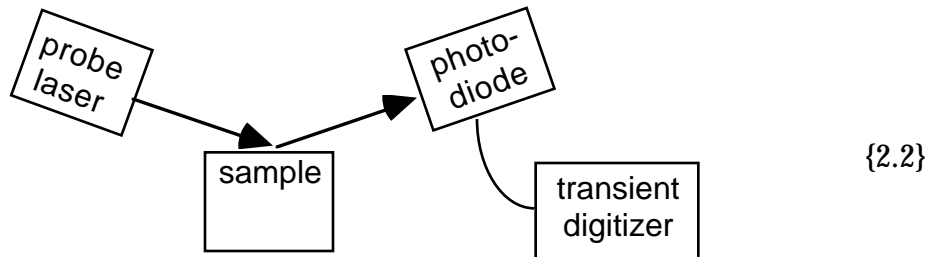
The exact solidification rate depends largely on the details of the energy deposition and thermal diffusion. To achieve as wide a range of solidification velocities as possible, we use different kinds of lasers (different energy deposition) and different temperature substrates (different thermal gradient). We use a total of four different lasers for melting: our XeCl excimer laser at Harvard University, two ruby lasers at Sandia National Laboratory, and a Nd:YAG laser at Cornell University. The lasers cover a wide range of average power with pulse energies from 0.2 to 2.0 joules and pulse durations from 3 to 50 nanoseconds. The lasers also represent both infrared and ultra-violet wavelengths, and hence different ways of coupling the optical power to the sample. The second way we vary the velocity is by changing the heat flow in the sample. The Harvard laboratory is equipped with a CO<sub>2</sub> laser directed towards the back surface of the sample. Heating the substrate for a couple of seconds prior to firing the excimer lowers the thermal gradient between the melt and the substrate, thereby lowering the solidification velocity.

A generalized setup for pulsed laser melting looks like figure 2.1.



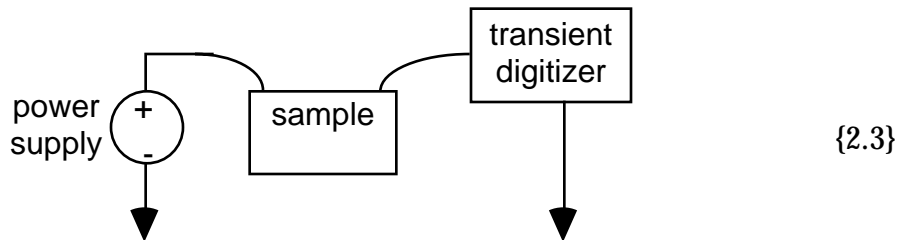
A nanosecond pulsed laser supplies energy to melt the sample. Focusing lenses compress the beam to give a high fluence. The homogenizer renders the beam spatially uniform and delivers it to the sample. There are three auxiliary systems (although not all are used in every experiment). The three systems are described here briefly, leaving the discussion of the measurements to chapter 3.

The first system, shown in figure 2.2, monitors surface reflectivity.



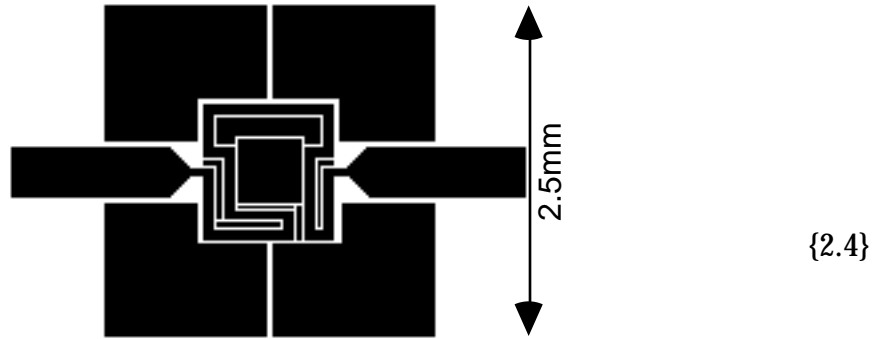
A fast photodiode such as EG&G's FND100 monitors the intensity of a low-powered probe laser reflected off the sample surface. The photodiode is part of a simple circuit that drives the 50Ω input of a transient digitizer with nanosecond time resolution such as a Tektronix TDS620. The photodiode is fitted with a narrow bandpass filter so that it sees only light from the probe laser.

A second system, shown in figure 2.3, monitors sample conductance.



A power supply biases the sample with 10 or 20 volts, and a transient digitizer monitors the voltage. Samples for conductivity measurements are photo-

lithographically patterned using the mask shown in figure {2.4}



The dark area of the mask becomes the area of the sample, and bare insulator is exposed in the white areas. The tabs on the left and right are covered with aluminum and annealed to provide ohmic contacts. The electrical path between the tabs snakes through the sample. The resulting high length-to-width ratio increases the signal-to-noise ratio of the conductance measurement.

A third system monitors the temporal profile of the melting laser. The setup is similar to that for monitoring surface reflectivity. The photodiode must be fitted with a narrow bandpass filter so that it sees only light from the melting laser. The laser intensity is high enough that the photodiode does not need to go directly in the path of the laser beam (if it is directly in the path, the beam must be attenuated or it will melt and destroy the photodiode). Also, we use an FND100Q photodiode to measure the profile of the excimer lasers; it has a quartz (Suprasil<sup>®</sup>) window that will not fluoresce in the ultraviolet light.

### 2.3.1 The Harvard Lab

The laser lab at Harvard (XeCl excimer laser, argon ion probe laser, CO<sub>2</sub> laser, other equipment, setup, calibration, laser control, substrate heating) is well described in Smith's thesis [Smith, 1992]. We have made only two significant changes since then. The first change is replacing the two Tektronix 7912AD transient digitizers with a Tektronix TDS620. The second is renovating the laboratory space. The lab setup itself changed little, but the room is completely new. One benefit of the changes is that electromagnetic noise is substantially reduced.

To make the experimental conditions match the assumptions of the model, we pay particular attention to the spatial homogeneity of the incident laser beam. Excimer lasers have a profile that is nominally a top-hat. The beam homogenizer is to make the profile a true top-hat. It breaks the laser beam into 49 pieces and recombines the pieces on surface of the sample to average out variations in intensity. At Harvard, we have two methods of checking beam uniformity: a CCD camera sensitive to ultraviolet light, and simultaneous reflectivity measurements.

The CCD camera, a Pulnix<sup>®</sup> TM-745E, is part of setup sold by Coherent Laser<sup>®</sup> specifically designed for measuring spatial profiles. Because the setup can operate at about one frame per second, it is a good tool for tuning the laser. Our experience is that a good tuning is 3% root mean square (RMS) deviation in pixel levels across a two by three millimeter oval area on the surface of the sample (the size of the oval corresponds to the area giving rise to the RBS signal). Over the course of a few days use, the homogeneity decreases to five percent RMS, at which point we tune the laser again.

Twin reflectivity measurements are much slower, but more meaningfully translated into error bars for data collected during the experiment. We split the probe beam into two parts, focusing on the middle of the sample, and moving the other beam around the sample. The intensities of the two reflected beams are measured by two photodiodes. Section 3.3 describes the reflectivity measurements. For a perfectly homogenous beam, the melt duration would be identical everywhere on the sample. By using two beams at once, we can measure the ratio of laser intensity at any point on the sample with respect to the center of the sample. Statistical analysis of many measurements is a direct determination of the error in the actual measurement due to excimer laser non-uniformity.

Table 2.3 summarizes a typical series of twin reflectivity measurements. The variation in melt duration across the sample was  $\pm 4\%$ , a value that indicates properly aligned optics. On this particular day, the top was warmer than the bottom. and the left slightly warmer than the right. Note that the center is 0.48% different than itself. This difference is the cumulative effect of the tightness of focus of the two probe beams, the accuracy with which the two probe beams could be placed in the same location, and particularities

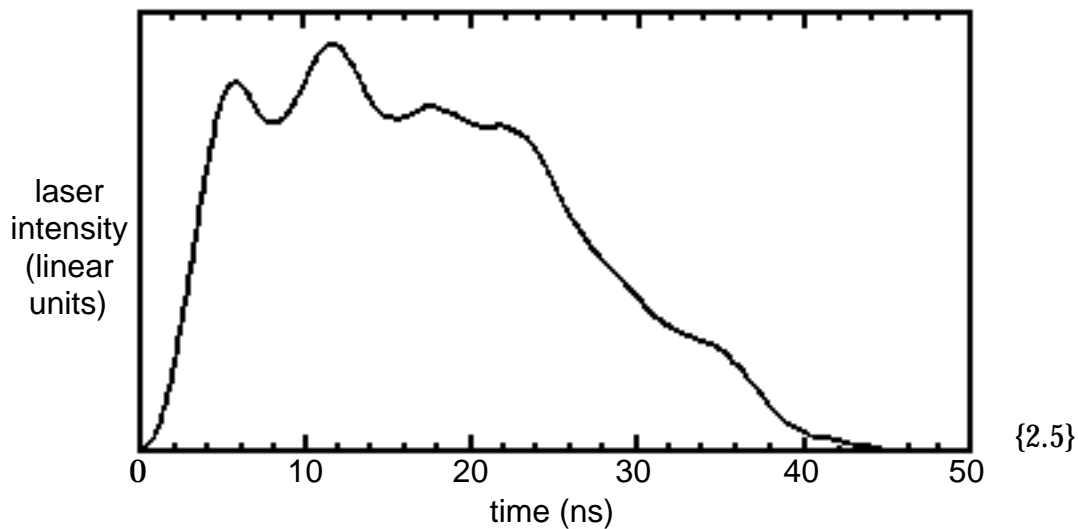
of the two detection circuits. Preheating with the CO<sub>2</sub> laser (when it is well aligned) does not increase the variation in melt duration beyond  $\pm 4\%$ . Thus, the  $\pm 4\%$  variation in melt duration is the uncertainty in measured melt duration due to spatial non-uniformity of the laser beam.

Table 2.3: Spatial uniformity of excimer beam

measured difference in melt duration relative to melt duration at the center

top left: -3.87%	top center: -2.25%	top right: -2.75%
center left: -1.39%	center: 0.48%	center right: 0.13%
bottom left: 1.36%	bottom center: 4.34%	bottom right: 3.14%

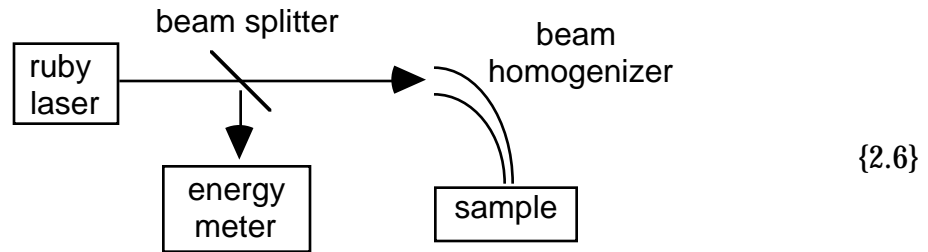
Another parameter describing the laser pulse is the temporal profile of intensity. Figure 2.5 shows the average of 25 consecutive measurements.



The pulse profile is very repeatable, both from shot to shot and from day to day. The ringing in the pulse corresponds to twice the length of the chamber in light-nanoseconds (it takes about 6ns for a photon to make a round trip between the reflectors in the laser cavity).

### 2.3.2 The Sandia Lab

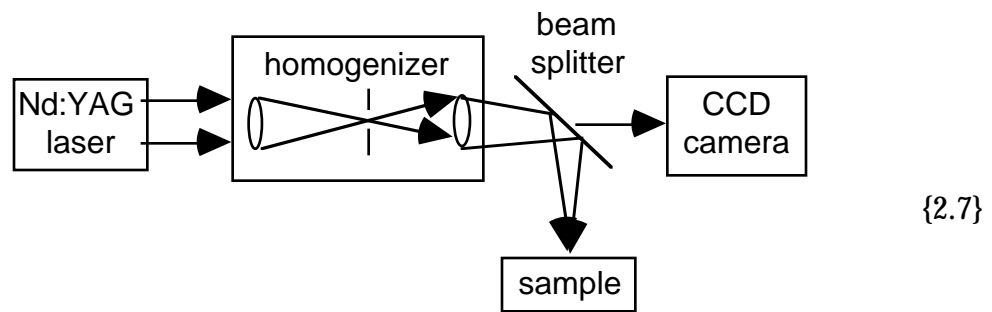
The two ruby lasers at Sandia National Laboratory were used for pulsed laser melting of the SOS samples. The setup is shown in figure 2.6.



Because the lasers have variable temporal profile and widely varying energy, both temporal profile and energy are measured for every pulse. The homogenizer is a bent quartz tube. The probe laser for surface reflectivity is a helium-neon laser.

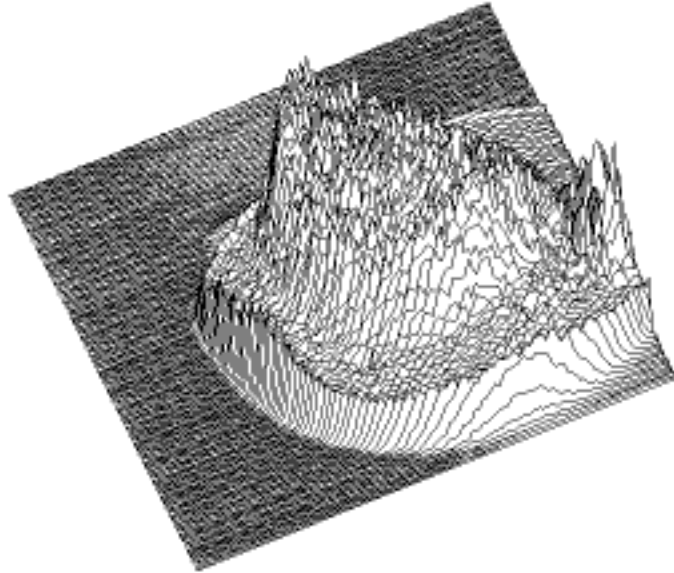
### 2.3.3 The Cornell Lab

The Cornell lab has a Nd:YAG laser, set up as in figure 2.7.



The higher temporal coherence of the beam complicates homogenization. The homogenizer has three elements: a lens that focuses the beam to a point, a low-pass spatial filter (pinhole) at the focal point of the first lens, and an exit lens to bring the diverging beam back to focus. The laser beam is intense enough to cause dielectric breakdown of air when focused to a point. To conserve laser power, the homogenizer is in vacuum and the sample is positioned before the focal point of the second lens. A beam splitter diverts a little of the beam to a beam profiler which simultaneously tracks beam uniformity and measures pulse energy (the energy was calibrated using an external pulse energy meter).

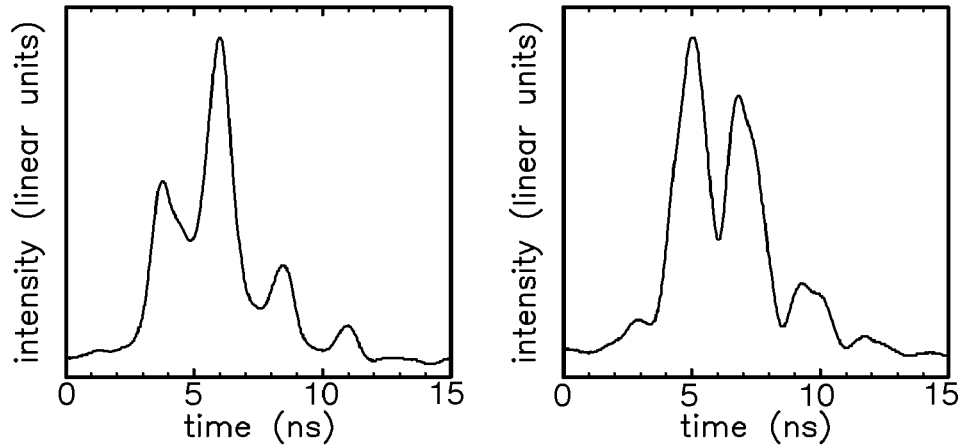
Pulses from the Nd:YAG laser have spatial intensity profiles that are Gaussian. We set up the laser so that the Gaussian is wide. The beam homogenizer makes the Gaussian smooth. Figure 2.8 shows the intensity distribution of a typical pulse as measured by the CCD camera.



{2.8)

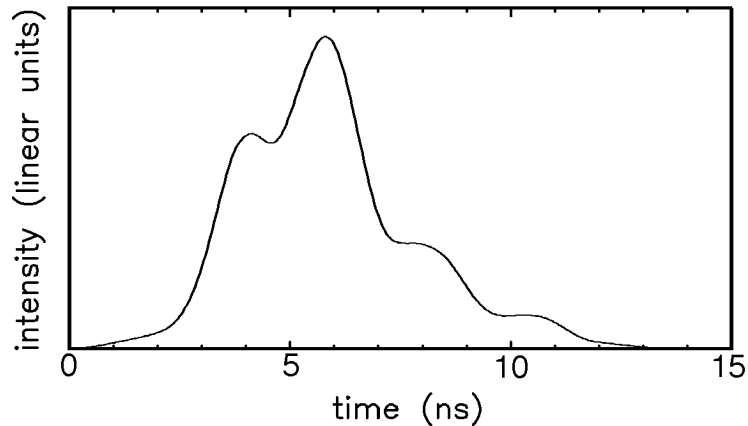
The intensity distribution over the area of the sample the size of the RBS beam spot is another component of error in the measurement. To calculate the error this introduces into the measurement, we need to relate the spatial and energy scales of the digitized camera image to the beam spot and energy on the sample surface. To calibrate the energy scale, we compare total counts in the image to the energy measured by a pulse energy meter placed where the sample sits. To calibrate the spatial scale of the image, we profile beam intensity at the plane of the sample using a pinhole of known diameter. We then numerically convolve the measured intensity profiles with a pin-hole shaped region of varying diameter (measured in pixels) until the spatial profiles match. The result is that over the area of the sample analyzed by RBS and electron microscopy, spatial inhomogeneity of the beam accounts for an uncertainty of  $\pm 1$  m/s.

The Nd:YAG has a temporal profile that changes from shot to shot. Figure 2.9a (left) and 2.9b (right) show the two basic shapes.



{2.9}

Even for pulses that have the same basic shape, there is variation in the location of the peaks. Figure 2.10 shows the average of 50 consecutive measurements.



{2.10}

Averaging smooths the profile, but because four-peak pulses are more common than three-peak pulses, the average pulse is four-peaked.

These same shapes appear in the surface reflectivity measurements. There are two ways in which part of the Nd:YAG pulse can get through the interference filter. The first is that the wavelength of the probe laser (a type 4412A diode laser at 780 nm) is too close in frequency to the Nd:YAG (1064 nm). The bandpass filter is not sharp enough to handle the intensity difference between the two lasers. The diode laser is milliwatts, whereas the peak Nd:YAG power is megawatts. The second reason for interference is heat radiated from the sample. The surface temperature of the sample during the Nd:YAG laser pulse goes well above the melting temperature of silicon.

## 2.4 Relation Between Theory and Experiment

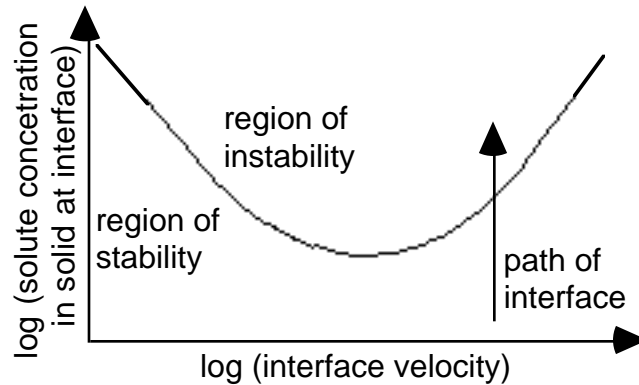
Stability theory calculates where a planar interface is stable, and where it is unstable. There are two approaches for experimentally testing the theory. The first is to look for the two regions: solidify samples in one region or the other. The second is to look for the boundary: solidify samples that pass from one regime to the other. This thesis contains data based on both approaches, but searching for the boundary is the better one.

In early stages, this experiment looked like a search by region. For example, measuring solute trapping requires that the interface remain planar; therefore, initially samples were prepared with doses of tin low enough to be far from the region of instability. None showed signs of breakdown, thereby confirming theory.

Our technique for rapid solidification does not allow us to make samples that never show signs of planar solidification. Because the laser intensity is spatially uniform, the interface always begins planar. Also, to obtain epitaxial growth, solidification must always begin with a good seed crystal. We obtain the seed by melting though the region of the sample damaged by the tin implant. Therefore solidification always begins at a point where the tin concentration is negligible. Without solute to drive the instability, the interface remains planar for the first part of solidification.

These two observations point out the limitations of searching by region. First, it is tedious to locate the neutral stability curve by exhaustively covering the region of stability. Second, we cannot have solidification in the unstable regions without crossing the neutral stability curve. Thus, almost all the data presented in chapter 5 consist of samples that cross the neutral stability curve into the region where the interface is unstable.

Consider the neutral stability curve of figure 2.11 (the oscillatory branch, which plays no role in the silicon-tin system, is not shown).



{2.11}

When the laser pulse ends, the interface rapidly reaches a velocity in the right hand side of the plot. Because the melt depth is deeper than the tin implant, the tin concentration is low, towards the bottom of the plot in the region of interface stability. The interface moves at a nearly constant velocity as determined by heat flow in the substrate. Soon it reaches tin that has diffused from the implant depth towards the maximum melt depth. The interface encounters an increasing tin concentration as it continues towards the surface. The path of the interface through concentration-velocity space is a ray straight up from the starting point. The interface remains planar as long as it is below the neutral stability curve. When it crosses the neutral stability curve, the perturbations are able to grow and deform the interface; it becomes non-planar and a cellular structure forms. We therefore take the neutral stability curve to be the interface velocity and concentration in the solid just before the cellular structure appears.

One complication is that the solute distribution may never reach steady state. Liquid phase diffusion of tin in silicon is fast, but between the maximum melt depth and the implant depth, the interface will still be climbing a gradient in solute concentration. Diffusion simulations (figure 3.2 for example) show that the solute profile between the implant depth and the surface is essentially level before solidification begins (at least for low implant doses). We expect the deviation from steady-state to underestimate the concentration at neutral stability (although we think the effect is a weaker than the rate of growth effect discussed below). An uphill concentration gradient will inhibit solute diffusion away from the interface, thereby increasing the excess solute at the solid-liquid interface. We address this

problem experimentally by analyzing different solute concentration gradients in the liquid.

The surface also presents a barrier to diffusion. The characteristic width of the solute peak in the liquid ahead of the interface is  $D/V$ , about 25nm for silicon-tin. By the time the interface is that close to the surface, solute diffusion away from the interface is substantially reduced. The build up of solute tends to lower the measured neutral stability point. We avoid this complication by ignoring samples where breakdown occurs within  $D/V$  of the surface.

A larger source of error is the finite amount of time that passes between the moment the interface first becomes unstable and the time the interface becomes so deformed that it creates microstructure large enough to be detectable. It is doubtful that linear response to infinitesimal perturbations can model an interface deformed to such an extent. The question strains even non-linear stability theory. (The literature is well developed. See for example the seminal paper of Wollkind and Segel [Wollkind and Segel, 1970] or the more recent work by Huntley and Davis which includes calculations for silicon-tin [Huntley and Davis, 1993b].) We assume that instabilities grow quickly. To the extent that we are wrong, we are over-estimating the concentration at neutral stability, because the interface will have passed neutral stability before we identify the instability.

# Chapter 3

## Interpretation of Data

### 3.1 Ion Scattering

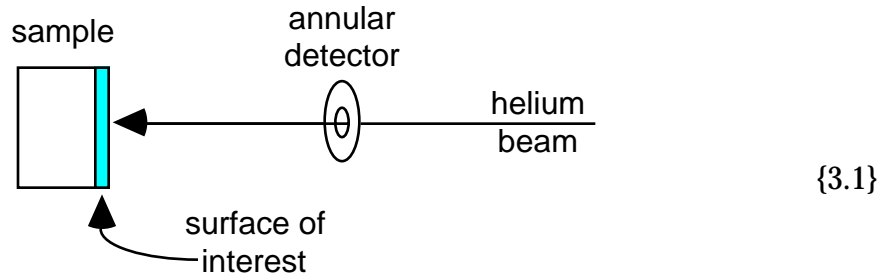
We use ion scattering techniques both as a quantitative measure of partitioning and as an indicator of interface breakdown. This section begins with an introduction to concentration profiling using Rutherford backscattering spectrometry (RBS). For more details, we refer the reader to Smith's thesis [Smith, 1992]. The second part of this section discusses how RBS measurements are interpreted to give the partition coefficient and liquid phase diffusivity. The third and fourth parts introduce ion channeling and its application as an indicator of interface breakdown.

#### 3.1.1 Measurement of Concentration Profiles

Rutherford backscattering spectrometry (RBS) is a powerful technique for measuring concentration profiles in the near surface region of a sample. The technique assumes lateral uniformity of the sample, a constraint fully compatible with sample preparation by ion implantation and with laser melting by spatially homogeneous laser pulses. Also, the technique distinguishes atoms based on mass, and thus distinguishes readily between silicon

and tin. The wide variety of tin isotopes found in nature poses no problem because ion implantation also includes isotope selection.

The raw data come from measuring the energy of helium ions scattered off the sample. Figure 3.1 shows the geometry.



A beam of 2MeV helium ions is collimated and directed at the surface of the sample. Some of the helium ions scatter off atoms in the sample. An annular detector measures the energy of ions scattered by approximately 176 degrees (nearly straight back). The raw spectrum is yield (number of events) as a function of ion energy.

The coarse energy scale is a mass scale given by

$$E_1 = k_{\text{RBS}} E_0 \quad (3.1)$$

where  $E_1$  is the energy of the backscattered ion,  $k_{\text{RBS}}$  the kinematic factor, and  $E_0$  the energy of the incident ion. The kinematic factor is like that for hard sphere scattering. In general it contains geometric factors, but for perfect ( $180^\circ$ ) backscattering, it simplifies to

$$k_{\text{RBS}} = \left( \frac{m_2 - m_1}{m_2 + m_1} \right)^2 \quad (3.2)$$

where  $m_2$  is the mass of an atom in the sample and  $m_1$  is the mass of the helium ion (4amu). The fine energy scale is a depth scale. The energy difference between an ion scattered off the surface of the sample and an ion scattered within the sample relates to the distance the ion travels through the sample. Because the two scales have different dependencies on the geometry, they can be unambiguously separated by comparing spectra collected at different sample tilts. For tin in silicon, tilting is not necessary because the masses are quite different:  $m_2$  is 28amu for silicon ( $k_{\text{RBS}}$  of 0.562) and  $m_2$  is 120amu for tin ( $k_{\text{RBS}}$  of 0.875).

We analyzed the spectra using Smith's SA program [Smith, 1992; Appendix B]. He describes the program in detail with particular attention to the underlying assumptions, algorithms, and user interface. The result of the analysis is a plot of tin concentration as a function of depth in the sample.

### 3.1.2 Application: Measurement of Partition Coefficients

For steady-state solidification, the solute distribution is that of equation 1.4 (sketched in figure 1.4). The features of the distribution are a constant bulk concentration and a peak at the interface. The amount of solute in the peak is obtained by integrating equation 1.4.

$$\int_0^{\infty} C_L(z') - C_{\infty} dz' = \frac{D}{V} \left( \frac{1-k}{k} \right) \quad (3.3)$$

Note that the area of the peak is determined by  $V$ ,  $D$ , and  $k$ . Because  $V$  can be determined by conductance measurements,  $D$  and  $k$  are the two unknowns. Outside of steady-state, equation 1.4 is no longer valid. We must solve the complete diffusion equation

$$\frac{dC}{dt} = D \frac{d^2C}{dz^2} \quad (3.4)$$

subject to the boundary conditions imposed by the surface and the moving solid-liquid interface. Figure 3.2 shows the results of a numerical solution to equation 3.4. The melt history, figure 3.2a, specifies the location of the solid-liquid interface (the moving boundary condition). For the first 35 or 40ns the sample is melting, reaching a maximum melt depth just over 4000Å. Then solidification begins; the interface soon reaches a velocity around 3.3 m/s. The sample has fully solidified 120ns. Figure 3.2b shows the evolution of the solute profile. The top of figure 3.2b shows the initial solute distribution (the result of ion implantation; solid lines represent solute in the solid). The distribution has a maximum of 3% at a depth between 300Å and 400Å. Time zero is when the sample begins to melt. After 15ns, the melt depth is close to 2000Å. The solute in the liquid (shown with a dotted line) diffuses, hence the implant peak spreads out. After 90ns, the sample has solidified to where only the top 2000Å remain molten. The solute concentration at 2500Å (the right hand edge of the plot) is practically zero, with a gentle increase up to 1.6% at the surface. As solidification continues (105ns, 120ns, and 150ns), solute accumulates in the liquid in

Figure 3.2  
Evolution of solute distribution during pulsed laser melting



front of the interface. If there is no interface breakdown, then a large amount of solute is zone refined all the way to the surface.

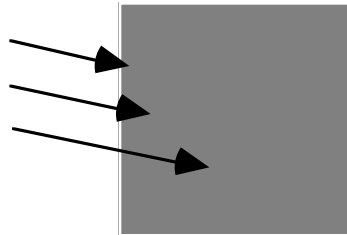
Smith [Smith, 1992] discusses the numerical techniques and software that we use to solve the diffusion equation (see Smith's section 3.3; the first version of the program was written by Michael Thompson at Cornell University). The amount of zone refining still depends on  $D$  and  $k$ , so we repeat the calculations with different  $D$  and  $k$  until we find a good fit. The two parameters are mostly separable, with  $D$  dominating the shape of the profile

below  $1000 \text{ \AA}$  and  $k$  dominating the shape in the top  $500 \text{ \AA}$ .

Among all the techniques for measuring concentration as a function of depth, RBS is the only quantitative method for measuring the concentration of impurity atoms in the surface peak normalized by the bulk concentration. This ratio is the crucial number for determining an accurate partition coefficient.

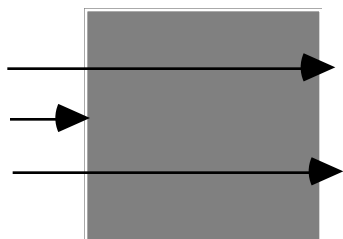
### 3.1.3 Ion Channeling Analysis

Feldman, Mayer, and Picraux [Feldman *et al.* 1982] discuss ion channeling techniques in detail. For most orientations of a crystal, ions arrive off-axis and see an array of atoms which fills space in a seemingly random fashion.



{3.3a}

However, for ions entering a crystal with a trajectory parallel to the rows of atoms, the odds of a backscattering event are greatly reduced relative to a trajectory of random orientation.



{3.3b}

There are two reasons. First, the open channels present a larger cross-sectional area than the rows of atoms viewed end-on. Second, the rows of atoms electrostatically steer the incident ions down the channels. For silicon, which has a rather open lattice, careful alignment of the crystal with the ion beam reduces the scattering yield to just a few percent of the off-axis yield.

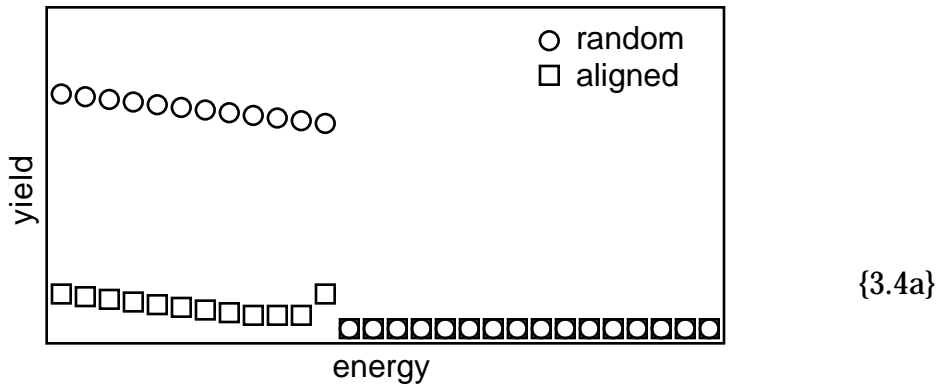
### 3.1.4 Application: Indication of Interface Breakdown

Determining whether or not the tin atoms are substitutional on the silicon lattice is a straight-forward application. One compares a spectrum collected with the sample aligned on a major crystal axis (the “aligned” spectrum) to a spectrum collected off-axis (the “random” spectrum). When a tin atom sits on a silicon lattice site, it has little effect on the channeling behavior. When off the lattice site, it constricts the channel. Thus, non-substitutional tin can be identified by its large scattering yield in the aligned spectrum.

The geometry for the ion channeling measurements is nearly the same as figure 3.1. When putting the sample in the vacuum chamber, we use a laser to align the sample surface normal with the incident beam. Because wafers usually have some miscut, the next step is to align the sample so that the incident beam is collinear with the principal crystallographic axis of the crystal, [100] for most of the samples. This is the geometry for the aligned spectrum. After collecting the spectrum, we tilt the sample five degrees and begin rotating it so that the incident beam sweeps out a cone around the principle crystallographic axis. The random spectrum is acquired during sample rotation; the rotation averages out other orientation effects such as planar channeling.

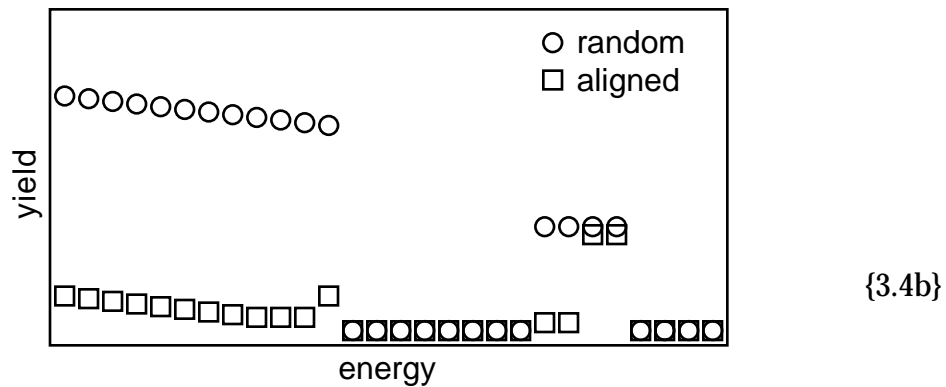
The spectra are analyzed by calculating the ratio of normalized yields  $\chi$  ( $\chi = \text{aligned}/\text{random}$ ) for both tin and silicon as a function of depth.

For clean, unimplanted, single-crystal Si(100),  $\chi$  is usually low, just a few percent after the first monolayer. Figure 3.4a shows schematized spectra.



For energies greater than  $k_{RBS}E_0$  (the sixteen channels on the right side of the figure) there is no scattering so the yield is zero. Below  $k_{RBS}E_0$  (the eleven channels on the left) the aligned yield is much less than the random yield, so  $\chi$  is small.

Figure 3.4b shows a schematized spectra of a sample containing tin.



Because  $k_{RBS}$  is greater for tin than for silicon, scattering from tin occurs at higher energies than scattering for silicon. In the figure, the tin peak is four channels wide. However, in the two channels on the left (the ones that represent signal from greater depth in the sample),  $\chi$  is small like for silicon; therefore the tin is substitutional. In the other two channels,  $\chi$  for tin is large. The relation between scattering yield and orientation is different for tin and for silicon; therefore the tin atoms cannot be substitutional on the silicon lattice.

For intermediate values of  $\chi$ , Feldman, Mayer, and Picraux [Feldman *et al.* 1982; page 59] give a first-order estimate for the fraction  $S$  of solute that is substitutional on the solvent lattice:

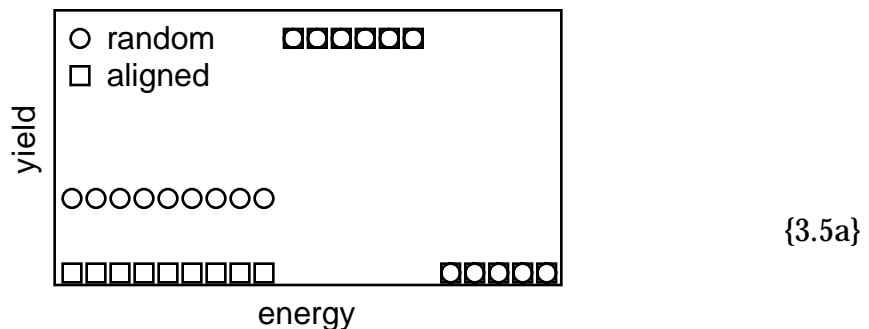
$$S = \frac{1 - \chi^{\text{solute}}}{1 - \chi^{\text{solvent}}} \quad (3.5)$$

The equation is an estimate because it assumes a uniform spatial distribution of the channeled beam and a uniform distribution of the non-substitutional tin in the sample. The first assumption is adequate, but in general cannot be met exactly because some fraction of the incident beam is steered into the channels. The second assumption is adequate in this experiment because the tin in cell walls probably exists as a non-oriented precipitates.

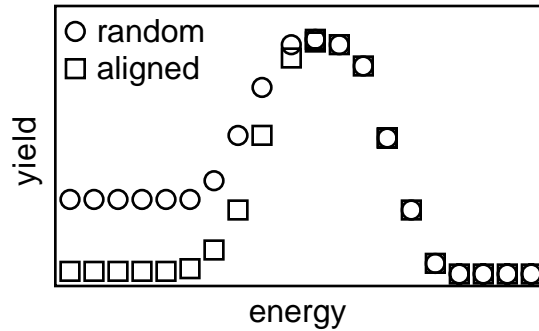
In collaboration with Patrick Smith, we modified the SA program to calculate  $S$  from random and aligned spectra (the modifications are documented in appendix A). When presenting spectra in chapter 5, we plot data two ways. For raw data, we use yield as a function of energy for both random and aligned spectra as in figure 3.4. For analyzed data, tin concentration as function of depth, we plot total concentration and substitutional concentration

$$C_{\text{substitutional}} = S \times C_{\text{total}} \quad (3.6)$$

Limited depth resolution complicates comparison of aligned and random spectra. Consider the spectra of figure 3.5, an expanded view of a tin peak. The total concentration is high near the surface and low a little deeper.



Deep in the sample,  $\chi$  is small; near the surface  $\chi$  abruptly increases. The interpretation is that the low concentration of tin went into solution, but the high concentration near the surface did not. The interface has undergone breakdown. We convolve this spectra with a Gaussian to simulate finite detector resolution and obtain



{3.5b}

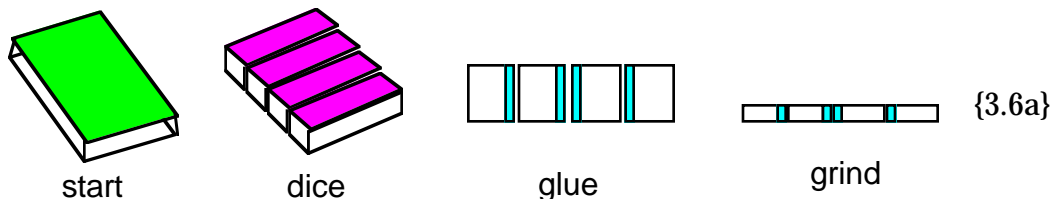
which no longer shows an abrupt transition. What value of  $\chi$  is significant? Also, is the breakdown really cellular? If it is not cellular, then the theory should not even apply. The spectra do not contain answers to these questions. Therefore we turn to a complimentary analytical technique, electron microscopy.

## 3.2 Electron Microscopy

### 3.2.1 Cross-sections

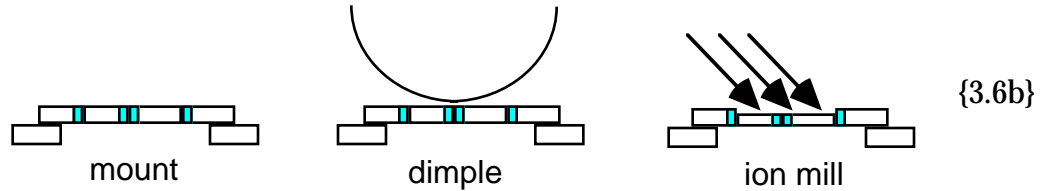
Cross-sectional transmission electron microscopy can confirm cellular breakdown and determine the depth at which the cells appear. The determination of depth is much more precise than in RBS. Comparing RBS and microscopy reveals what kind of spread between total concentration and substitutional concentration is significant, and therefore serves as a guide for interpreting RBS data from other samples.

We prepared a number of samples for microscopy using the following recipe.



- 0) Sample begins as a 3×5 mm rectangle.
- 1) Dice sample into bars.
- 2) Epoxy bars together using M-60<sup>®</sup> epoxy.

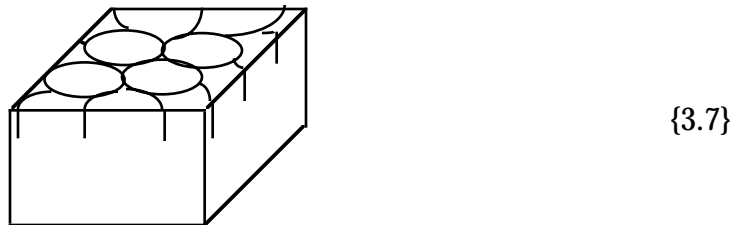
- 3) Mount on a polishing chuck using glycol phthalate.
- 4) Grind the sandwich with diamond paste to about 300 microns.
- 5) Polish with 0.05 micron alumina.
- 6) Flip the sample and polish the other side, leaving about 200 microns.



- 7) Mount on a copper grid using 5-Minute® Epoxy.
- 8) Dimple until the center is red when viewed in transmission.
- 9) Ion mill until the hole crosses the interface of interest.

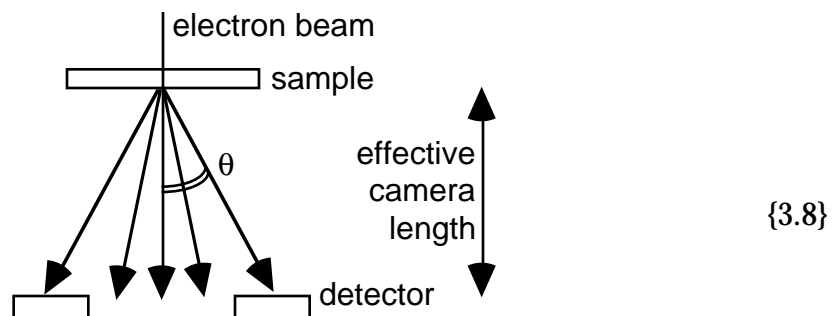
As shown in figure 3.6, the sandwich is constructed so that there are two surfaces of interest in the middle of the sample.

The breakdown mode in silicon-tin is cellular. Cell boundaries run perpendicular to the surface down into the sample as shown in figure 3.7.



In cross-section, cell boundaries look an irregular array of streaks hanging down from the surface. The length of the cell wall corresponds to the depth of breakdown. The source of contrast is variations in diffraction conditions due to tin precipitates in the cell wall and defects in the nearby silicon.

Atomic number contrast (“Z-contrast”) microscopy [Pennycook and Narayan, 1984; Pennycook, 1989] requires the setup of figure 3.8.



A scanning transmission electron microscope (STEM) rasters the electron beam, measures the intensity transmitted through the sample, and builds the image pixel by pixel on a computer screen. One of the available electron detectors is annular. Because the electron beam is incident at a constant tilt angle (normal incidence in figure 3.8), the annual detector allows dark field imaging. For Z-contrast imaging, the STEM is setup so that only electrons scattered through extremely large angles reach the detector. The hole in the detector is 2mm in diameter and the effective camera length of the microscope is set at 60mm. Therefore the detector collects electrons that are scattered through angles greater than  $\theta = \tan^{-1}(2/60) = 35 \text{ mrad}$ . This is a large scattering angle compared to regular transmission electron microscopy. The lowest order diffraction spot that contributes to the image is the (9 9 11) peak. At such an angle, Rutherford forward scattering is the dominant mechanism (for pure Rutherford scattering, Pennycook recommends an angle greater than 80mrad). The image intensity is proportional to

$$\sum n_i Z_i^2 \tag{3.7}$$

where  $n_i$  is the number of atoms of element  $i$  in the sample under the electron beam and  $Z_i$  is the atomic number of element  $i$ . Because the electrons that make up the image are incoherent, image interpretation is simple: areas of higher mass appear brighter.

Figure 3.9 demonstrates the dependence on camera length (the magnification is about  $\times 10^5$ ; the scale bar is  $0.5 \mu$ ). Both the top and bottom micrographs show the same area of the same sample. The only difference between the two is the STEM's camera length. The sample tilted was chosen so that no bright diffraction spots from the single-crystal silicon film contribute to the image. The silicon is therefore gray, modulated by defects which diffract differently. The sapphire (at the very bottom of the micrograph) is a more uniform gray because it has fewer defects. The top micrograph, taken with a camera length of 60 mm, is a Z-contrast image. Almost all diffracted and undeflected electrons pass through the hole in the center of the detector. The lower micrograph is take with a more normal camera length, 240 mm. Diffraction from defects, particularly the twin defects coming up from the silicon-sapphire interface, is now obvious. There are also speckles near  $1500 \text{ \AA}$ , implant damage not erased by melting.

Figure 3.9  
Role of camera length in Z-contrast imaging  
The scale bars are 0.5  $\mu\text{m}$ .



We use Z-contrast microscopy to verify cellular breakdown in the SOS samples. The lattice mismatch between sapphire and silicon results in a high number of twin defects near the silicon-sapphire interface. When the sample melts to the depth of these defects, the melt solidifies with twin defects and dislocations. These defects in turn give rise to diffraction contrast that is similar to the contrast from cell walls and often masks the beginnings of cell walls. Atomic number contrast microscopy identifies cells walls based on a higher than average concentration of tin. Being insensitive to diffraction effects, Z-contrast microscopy allows us to sort out which features are due to tin precipitating and which are due to poor epitaxy caused by extended defects at the maximum melt depth.

The possibility that poor epitaxy is seeding interface instability [Morris and Winegard, 1969] makes it important to verify observations in SOS with observations in bulk silicon. The advantage of bulk silicon is that it is practically defect-free. The disadvantage is that we cannot make conductance measurements (see section 3.4). However (see section 3.5), we can overcome this limitation by measuring the maximum melt depth. Therefore, following the example of Narayan *et al.* [Narayan *et al.* 1983] we build a marker into the sample that can be seen when doing cross-sectional transmission electron microscopy on the samples. The marker is a low-dose boron implant that creates point defects and dislocation loops deep in the sample. During laser melting, loops that melt disappear forever; loops that do not melt coarsen to a size large enough to see in the microscope (several hundred angstroms). The maximum melt depth is therefore the depth at which the sample changes from having no loops to having many loops. The maximum melt depth is sharply defined. Because dislocations cannot have free ends inside the crystal, loops that half melt must seed dislocations that go to the surface. Narayan occasionally saw such threading dislocations, strong confirmation that dislocation loops exist in the unmelted solid right up to the maximum melt depth.

### **3.2.2 Plan View**

One sample was prepared for plan view transmission electron microscopy. The sample was made by mechanical grinding and chemical

polishing. The mechanical part consisted of:

- 1) cutting a 3 mm disk out of the center,
- 2) grinding the backside to reduce the thickness to less than 0.5 mm, and
- 3) dimpling a shallow depression in the back.

The chemical part consisted of:

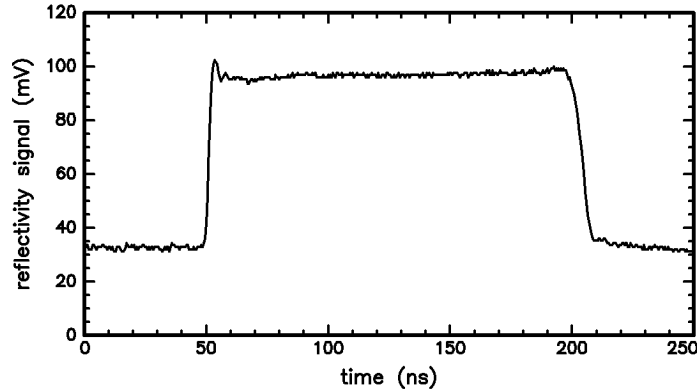
- 4) mounting the sample face down on a glass microscope slide,
- 5) protecting the sides with wax, and
- 6) etching in 12:1 solution of  $\text{HNO}_3$  and HF until the sample transmitted red light.

The sample was then cleaned in solvents and milled in an ion miller.

### 3.3 Measurement of Melt Duration

Section 2.3 describes the use of a probe laser, fast photodiode, and transient digitizer to monitor the surface reflectivity of the sample during pulsed laser melting. The goal is to measure the melt duration. For silicon samples, the large difference in optical properties between the solid and liquid makes the measurement straight forward. Liquid silicon is a metal; solid silicon is a semiconductor. We exploit the difference in two ways. First, the two phases have substantially different reflectivities: high for the metallic liquid and moderate for the semi-conducting solid. This alone provides a clear signal. Second, we obtain additional contrast by using polarized light incident at the Brewster angle. If solid silicon were an ideal dielectric, no light would be reflected at that angle of incidence and angle of polarization. In practice, the reflectivity at the correct angle of polarization is just a few percent of the reflectivity of the orthogonal polarization. Once the sample surface melts, it is no longer a dielectric, so the attenuation due to the Brewster effect disappears. In total, we see the reflectivity signal change by a factor of 3 when the sample melts.

Figure 3.10 shows a typical reflectivity measurement for a silicon-tin sample.



{3.10}

We take the melt duration to be the full width at half maximum of the peak. One feature is the difference in reflectivity between the left and right sides of the plot. The left side is the reflectivity of the room temperature solid, and the right side is the temperature of the hot solid. Another feature is the rise and fall times for the peak. In theory, the detection circuit has a rise time less than 3 ns. Observed rise times (melting transition) are limited by the electronics. Observed fall times (solidification transitions) are longer because of the amount of time required to solidify the volume of sample giving rise to the signal [MacDonald *et al.* 1988]:

$$\frac{\text{skin depth}}{\text{velocity}} \sim \frac{10 \text{ nm}}{1 \text{ nm/ns}} = 10 \text{ ns.} \quad (3.8)$$

Even longer fall times indicate problems, such as grossly non-uniform solidification. We exclude such samples from further investigation.

### 3.4 Measurement of Velocity I: Transient Conductance

Transient conductance measurements [Galvin *et al.* 1982; Thompson *et al.* 1983] are the most accurate means for determining solidification velocities in the meter per second regime. Smith [Smith, 1992; see section 2.2] gives an excellent discussion of the technique. In the analysis, the solid and liquid layers are modeled as resistors in parallel. Knowing the resistivity of the solid and liquid, the physical dimensions of the sample, and the electrical characteristics of the measuring circuit, we can derive an equation relating measured conductance (as a function of time) to melt depth. The technique works well for SOS samples because even small amounts of liquid

silicon change the sample conductivity dramatically; the conductivity of the solid (a semiconductor) and of the liquid (a metal) differ by a factor of thirty at the melting point [Gibson, 1960]. For the highest implant doses ( $3 \times 10^{16}$  and  $1 \times 10^{17}$   $\text{cm}^{-2}$ ), the conductance measurements are difficult to interpret, so we do not use these samples for data. Thus all the velocities reported here for the SOS samples are reliable numbers based on good conductance measurements.

Although SOS offers direct measurement of velocity, its disadvantage is a high density of extended defects in the silicon film. We attempted to make samples that had lower defect densities yet retained the advantage of direct measurement of velocity. Our results were unsuccessful. We think there is no ideal sample, only an essential trade-off between unwanted defects and unwanted conductance. The intense laser radiation required to melt the sample also injects many photocarriers. These carriers can survive much longer than the melt and contribute significantly to the overall sample conductivity. For SOS samples, the silicon film is thin enough that the photo-carriers are quickly annihilated by the melt and the defects at the silicon-sapphire interface.

Our hypothesis that there is a trade-off is built on experience with two other kinds of samples. The first was bulk silicon with a silicon implant. The idea was that we could add defects at a depth where they trapped photocarriers then disappeared into the melt. Figure 3.11 shows the results. The melting has an obvious effect on conductivity, but a relatively minor one. The dominant contribution to conductivity is still photocarriers. The second alternative was silicon-on-insulator (SOI) with a nearly single-crystal silicon film. The conductance measurements were good, but not as good as on SOS. Also, although SOI was nearly single crystal, the defects that were present made ion channeling difficult. We eventually concluded that the exceptionally low defect density of bulk silicon was too attractive to pass over.

Another way to obtain solidification velocities is by matching measured melt durations to heat flow simulations. Simulations have an uneven reputation however because of early studies published before the optical and thermal properties of ion-implanted amorphous silicon were well established. The technique has been shown to be powerful and accurate for bulk silicon [Aziz *et al.* 1985], but care is required when applying the technique

Figure 3.11  
Typical measurement of bulk silicon conductance



to other systems. For example, simulation of SOS samples requires assumptions about the thermophysical properties of the sapphire, about the silicon-sapphire interface, and about the highly defective silicon region near the sapphire. Furthermore, although simulations of self-implanted silicon compare well with electron microscopy observation [Aziz *et al.* 1985], our samples are implanted with tin. Comparing simulated and measured curves of melt duration as a function of fluence for SOS samples, we find that the results are increasingly divergent as the tin dose increases. The conductance measurements are the correct ones. There are relatively few assumptions in the analysis, and the most crucial one, that the added tin not affect the conductivity, is good because tin and silicon both have four valence electrons. The conductance measurement also passes three important practical tests. First, the melt duration agrees with that determined by surface reflectivity. Second, the maximum observable melt depth agrees with the thickness of the entire silicon layer (the sapphire does not melt). Third, the shoulder on the conductivity trace during melting corresponds to the thickness of the amorphous layer created by the ion implantation.

In the next section we show how to use heat flow simulations properly. For example, the kind of comparison between simulation and measurement made above is sensitive to surface optical properties. If the implant changes the surface reflectivity by two percent, from 0.68 to 0.70, the absorbed energy ( $1-R$ ) changes by  $0.02/0.32$  or about six percent. Before using heat flow simulation, we need to examine the effects of implantation and determine robust quantifiers.

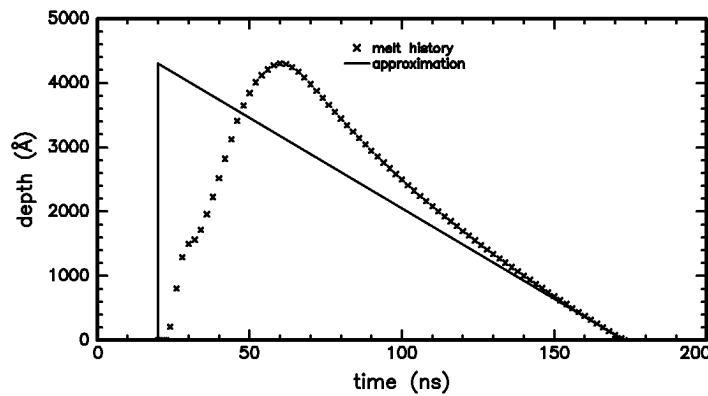
### **3.5 Measurement of Velocity II: Microscopy and Simulations**

Not all samples were prepared for transient conductance measurements. Therefore, we need a reliable method for obtaining velocities from heat flow simulation. (Parameters for all the heat flow simulations are given in Appendix B.) By implanting boron and examining sample cross-sections in the electron microscope, we can measure the maximum melt depth as well. In section 3.5.1, we use this information to estimate velocity.

In 3.5.2, we show that for silicon melted with the XeCl excimer laser without CO<sub>2</sub> heating, the estimate confirms simulation. Thus, simulation is a reliable tool for calculating accurate solidification velocities. We will use it for most of the results presented in chapter 5.

### 3.5.1 Estimating Velocity

Given the melt duration and maximum melt depth, dimensional analysis implies we have an estimate of velocity. Dividing depth by duration gives the approximation of figure 3.12.



{3.12}

This estimate is consistently low, because the melt duration includes the period of time in which the sample melts. We can improve the estimate by subtracting off the amount of time it takes the sample to reach the maximum melt depth. The maximum melt depth will occur approximately when the rate the laser puts heat into the melt equals the rate at which heat flows from the melt into the substrate. The heat flow is limited by the thermal conductivity of the hot solid at the interface and the thermal gradient. Using values of from table 2.1,

$$\begin{aligned} K_S G_S &= 22\text{W/Km} \times 1.9 \times 10^8 \text{K/m} \\ &= 4.2 \times 10^9 \text{W/m}^2 = 0.42 \text{MW/cm}^2. \end{aligned} \quad (3.9)$$

The average XeCl laser fluence is

$$(1.5\text{J/cm}^2) / (35\text{ns}) = 43 \text{MW/cm}^2. \quad (3.10)$$

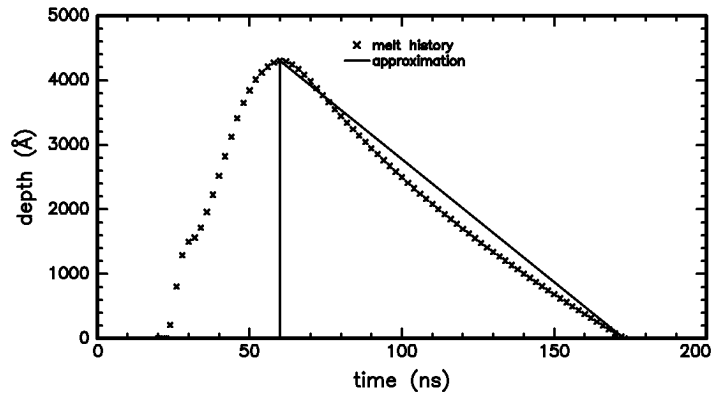
The laser power is overwhelming, so the sample begins melting almost as soon as the laser pulse begins, and it continues melting almost until the laser pulse ends; then solidification begins. Figure 4.1 (an SOS experiment) is typical. The sample reaches peak conductance at the maximum melt depth

because that is when the proportion of (metallic) liquid is the highest. Indeed, the maximum conductivity occurs near the end of the laser pulse.

Thus, our second estimate for velocity is

$$\text{velocity} \sim \frac{\text{maximum depth}}{\text{melt duration} - \text{pulse duration}} \quad (3.11)$$

Figure 3.13 shows this approximation graphically.



{3.13}

Table 3.1 shows the results obtained by applying the approximation of equation 3.11 to four bulk silicon samples (chosen because the CO<sub>2</sub> laser was not used and the maximum melt depth was measured by cross-sectional transmission electron microscopy).

Table 3.1

Solidification velocities for bulk silicon samples estimated using equation 3.11

sample name	melt duration (ns)	maximum depth (Å)	velocity (m/s)
IS04-184	143	3500	3.25
IS03-247	98	2300	3.65
IS10-04-01	150	4500	3.9
IS06-075	84	2000	4.1

The melt duration was measured by surface reflectivity. The maximum melt depth was measured by TEM. For equation 3.11, the pulse duration was 35 ns.

### 3.5.2 Comparison with simulation

How does this data for bulk silicon compare to simulation? (Parameters for all the heat flow simulations are given in Appendix B.) We first discuss two effects of implantation: it makes the sample surface amorphous and it turns it into an alloy.

The effect of an amorphous surface layer is well understood from experiments on self-implanted silicon [Aziz *et al.* 1985]. Accurate simulation requires using the optical and thermophysical properties of amorphous silicon. The change in properties creates noticeable features in the simulation when the solid-liquid interface moves from the amorphous region to the crystalline region. For SOS samples, one sees features in the conductivity traces too. No such features are obvious in the plots of melt duration as a function of laser fluence for the bulk silicon samples. Figure 3.14 shows an ion channeling measurement of the thickness of the amorphous region. The spectrum shows a continuous transition from amorphous to undamaged silicon (the slope is more gradual than the detector resolution), whereas samples implanted at liquid nitrogen temperature (like the SOS samples) show an abrupt transition. We would therefore like a way to plot the simulation results so they are not sensitive to the thickness of the amorphous layer.

The second effect is that implantation turns in the sample surface into an alloy. Figure 3.15 shows three plots of simulation results for bulk silicon with zero, 1300 Å, and 1600 Å of amorphous silicon on top. Figure 3.15a, maximum melt depth as a function of melt duration, is what is required. The two curves overlay in figure 3.15a because duration and depth both depend on the absorbed fluence. In figures 3.15b and 3.15c, the independent variable is incident fluence. The curves do not overlay because the incident fluence contains no information about the absorbed fluence.

The effect of alloying is more complicated. There are two cases: changing the optical properties of the thermophysical properties. Jellison, Modine, White, Wood, and Young [Jellison *et al.* 1981] have measured the optical properties of silicon heavily doped with boron. The doses we use are much lower, but because optical coupling depends in part on free carriers, low dose implants may have a noticeable effect. The thermophysical properties

Figure 3.14  
Ion channeling spectrum of silicon implanted at room temperature

Figure 3.15  
Heat flow simulations of silicon with an amorphous surface layer



**Figure 3.16**

**Measured melt duration as a function of laser fluence for various implants**

**3.16a: set of twelve implants (top)**

**3.16b: selected implants with same tin dose (bottom)**



(like latent heat) are less likely to be changed, but the effect may be noticeable for the higher dose tin implants.

Consider figure 3.16a, a melt duration as a function of fluence for twelve implants. Some implants are substantially different from the others. Figure 3.16b isolates a few implants that show the effect of varying the boron dose at constant tin dose ( $1e16\text{cm}^{-2}$  at 165 keV). The spread is substantial. Samples with higher near-surface concentrations of boron consistently have longer melt durations. The curves look parallel, but we are unable to fit the curve by simply changing the liquid reflectivity. Fitting would be even more difficult if the reflectivity varied during the experiment due to boron diffusion through the liquid to the surface. We have decided to throw out data from the extreme implants instead of analyzing them in more detail.

Figure 3.17a highlights a few implants showing the effect of varying the tin dose at constant boron dose ( $3e15\text{cm}^{-2}$  at 100 keV and  $5e15\text{cm}^{-2}$  at 200 keV). The spread here is much less, and no trend is evident. We take this as inherent scatter in the measurement: variation from implant to implant causes an uncertainty equivalent to  $\pm 5\text{ns}$ . Although the Si(100) data show no trend, figure 3.17b shows a tin dose effect for the Si(111) samples. Note too that these are higher tin doses, as high as those doses that gave unusual conductance measurements. The experiment is impossible at lower doses however. The ease of solute trapping in Si(111) makes it harder to accumulate enough excess solute in the melt to make the interface unstable. We must accept an error equivalent to  $\pm 8\text{ns}$ .

With these warnings about using fluence as an independent variable, we look at the advantages of simulation. Figure 3.18 shows several simulations of a XeCl laser pulses melting a sample that is  $1600\text{\AA}$  of amorphous silicon on silicon. The temporal profile of the laser pulse is the one shown in figure 2.5; it was scaled vertically to represent the various laser fluences. The laser pulse intensity is plotted with an arbitrary vertical scale along with melt depth as a function of time for each simulation. The maximum melt depth occurs late in the laser pulse as expected. It also moves back in time as the fluence increases, the effect of finite heat flow rate from the surface through the liquid towards the interface.

Figure 3.17  
Measured melt duration as a function of laser  
fluence for various tin implants  
3.17a: Si(100) with constant boron dose  
3.17b: Si(111) with no boron



Figure 3.18  
Heat flow simulations of silicon with a 1600Å amorphous layer on the surface

Simulation improves upon the estimate of equation 3.11 for shorter melt durations by taking into account the pulse shape and the time it takes to heat the surface to melting. For the longer melts, simulation improves the estimate by taking into account the heat flow rate through the liquid. Another observation about figure 3.18 is that the solidification velocity decreases slightly during solidification. As thermal diffusion broadens the thermal profile, the temperature gradient in the solid decreases as

$$G_S \sim \frac{1}{\sqrt{A_s t}} \quad (3.12)$$

and the interface velocity decreases. Also, hot silicon has a lower thermal conductivity than cold silicon. When quoting simulated velocities, we uniformly choose the velocity at 500 Å because that is a typical depth at which we observe cellular breakdown.

Figure 3.19 compares the data of table 3.1 to simulated velocities. The solid line is a fourth order polynomial fit through eleven simulations (circles along the curve). The four x's are the estimates of table 3.1. The agreement is good, thus simulation is a valid tool for experiments using the XeCl excimer laser without CO<sub>2</sub> heating.

**Figure 3.19**  
**Comparison of simulated and measured solidification velocities**

Table 3.2 compares simulated and measured maximum melt depths. For three out of four cases, the two depths agree to within 15%. This is reasonable agreement considering the sensitivity of the calculation to the exact laser pulse temporal profile and the thickness of the amorphous layer. The thickness of the amorphous layer plays a large role for the two samples with short melt durations which melted only a little past the depth damaged by implantation.

Table 3.2  
Comparison of measured and simulated maximum melt depths

sample name	melt duration (ns)	measured depth (Å)	simulated depth (Å)
IS06-075	84	2000	2300
IS03-247	98	2300	3000
IS04-184	143	3500	4100
IS10-04-01	150	4500	4400

Column 1 is the name of sample and implant

Column 2 is the melt duration measured by surface reflectivity

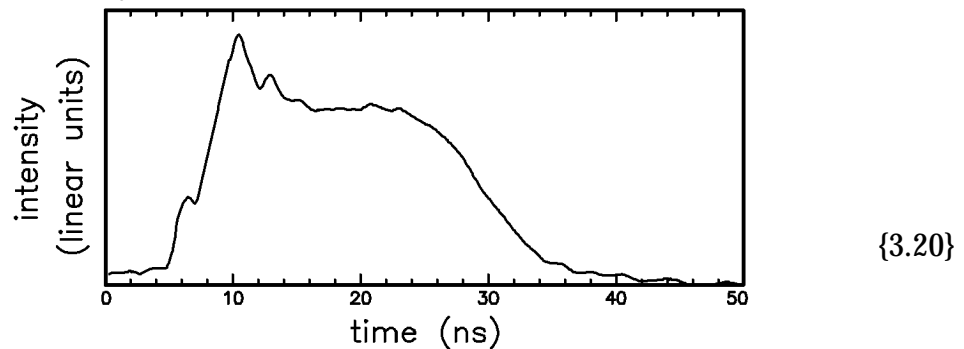
Column 3 is the maximum melt depth determined from microscopy

Column 4 is the maximum melt depth calculated by heat flow simulation

Simulations of samples preheated with the CO<sub>2</sub> laser have substantial error because we have no independent measure of the initial substrate temperature. The CO<sub>2</sub> pulse is not reproducible enough for us to predict the temperature. As an input to the simulation, the best we can do is fix the laser fluence, then vary the temperature until the simulation gives the measured melt duration. By introducing fluence as an independent variable, we introduce the level of error of figure 3.15b. Fortunately, the approximation of equation 3.11 is accurate for longer melt durations because moving the

instant of the maximum melt depth by five or ten nanoseconds in either direction will hardly change the velocity. Also, the temperature gradient is lower initially, so the rate of thermal broadening is lower than for shorter melts. Thus when using the CO<sub>2</sub> laser, we will always calculate the solidification velocity using equation 3.11 (and doing microscopy to get the melt depth).

So far, this discussion has focused on simulation of XeCl laser melting experiments. Simulation of bulk silicon samples melted with the Nd:YAG laser pose some different problems. The first is that the literature contains no quantitative study like that of Aziz *et al.* [Aziz *et al.* 1985] examining the simulation parameters for Nd:YAG pulsed laser melting. We will present a similar but quick examination in section 5.3 (and conclude that simulation is adequate). The second problem is that there is uncertainty in the measurement of melt duration, the independent variable that points towards velocity. As shown in the surface reflectivity measurement of figure 3.20, the profile of the Nd:YAG pulse masks the location of the melting transition in the surface reflectivity measurement.



Based on experience with frequency doubling of the Nd:YAG and experience with other probe lasers, we estimate that the sample melts halfway though Nd:YAG pulses. This is significantly different from XeCl pulses where the sample melts just after the pulse begins. Therefore, when applying equation 3.11 to samples melted with the Nd:YAG, one must use

$$\text{velocity} \sim \frac{\text{maximum depth}}{\text{melt duration} - \text{half of pulse duration}} \quad (3.13)$$

The idea common to both equations 3.11 and 3.13 is that the melt does not start to solidify until the laser pulse ends. The appearance of the Nd:YAG pulse in the measured surface reflectivity is not a much of a problem as it first

seems because the trace indicates both the end of the laser pulse (the beginning of solidification) and the end of the solidification.

Experiments done with the ruby laser suggest that equation 3.13 is quite accurate. In the ruby experiments, we simultaneously measure the intensity of the melting laser and the sample conductance and reflectivity. Table 3.3 shows typical data for seven SOS samples representing a variety of ruby pulse widths from those as short as the Nd:YAG to those much longer than the excimer. The velocities determined from conductance measurements are mostly 20% greater than the maximum melt depth divided by the melt duration and 10% lower than the estimate of equation 3.13. The 10% error is quite acceptable.

Table 3.3  
Solidification velocities for SOS sample estimated using equation 3.13

sample	laser pulse fwhm (ns)	melt duration (ns)	maximu m melt depth (nm)	V cond. (m/s)	$\frac{\text{depth}}{\text{time}}$ (m/s)	V Eq. 3.13 (m/s)
Sn3e15_01	3.5	12	100	10.5	8.3	11.8
Sn1e16_02	3.5	19	140	8.6	7.4	9.0
Sn8e15_04	3.5	25	175	8.0	7.0	8.1
Sn1e16_06	3.5	30	190	6.7	6.3	7.2
40Sn2_009	17	37	62	2.9	1.7	3.1
40Sn2_002	36	90	150	2.6	1.7	2.8
Sn3e15_07	20	230	450	2.2	1.9	2.1

Column 1 is the sample label.

Column 2 is the FWHM of the laser pulse (assume duration = 3×FWHM).

Column 3 is the melt duration measured by surface reflectivity.

Column 4 is the maximum melt depth determined from conductance.

Column 5 is the velocity determined from conductance measurement.

Column 6 is the melt duration divided by maximum melt depth.

Column 7 is the velocity calculated using equation 3.13.



# Chapter 4

## Solute Trapping in Silicon-Tin

When this experiment began, there were no measurements of solute trapping for silicon-tin in the literature. Therefore, we began by making these measurements using the standard techniques [Aziz *et al.* 1986; Smith and Aziz, 1994]. The results were published in an earlier paper [Hoglund *et al.* 1991]. For tin in Si(111), we use Reitano's data [Reitano *et al.* 1994].

The samples for the solute trapping experiment were (100)SOS wafers implanted with 100keV  $^{120}\text{Sn}$  to doses of 3 and  $5 \times 10^{15} \text{cm}^{-2}$ . The samples were melted by ruby laser pulses of 3 to 40 ns full-width-at-half-maximum duration and 0-5 J/cm $^{-2}$ . The fluences were chosen so that the region damaged by the implants would fully melt, but that the maximum melt depth would be less than the film thickness. The silicon that did not melt served as a crystallographic template for the solidification. The conductance measurements provided a direct measurement of melt history. Figure 4.1 shows data collected during a typical experiment.

Figure 4.1  
Pulsed laser melting of a SOS sample

Numerical simulations were then performed with various values of partition coefficient and liquid diffusivity until the initial solute profile evolved into the final solute profile in the time allowed by the measured melt history. Results for different samples were harmonized by choosing an overall best liquid diffusivity and fitting again for the partition coefficient. The values of liquid diffusivity varied from  $2.0$  to  $3.0 \times 10^{-4} \text{ cm}^2/\text{s}$  with an average value of  $2.5 \times 10^{-4} \text{ cm}^2/\text{s}$ . Figure 4.2 shows a typical battery of simulations with fixed diffusivity and different values of the partition coefficient. A partition coefficient of  $0.35$  provides the best fit. (Higher  $k$  means more solute incorporation and less zone refining. Therefore the  $k=0.35$  curve is the second from the bottom at depths between  $0$  and  $400 \text{ \AA}$ , then second from the top at greater depths. The sample's average velocity was about  $8 \text{ m/s}$ .)

The partition coefficients found using a diffusivity of  $2.5 \times 10^{-4} \text{ cm}^2/\text{s}$  are plotted as a function of velocity in figure 4.3. Figure 4.3b is an magnified view of figure 4.3a. The data are well fit by the continuous growth model

$$k(v) = \frac{k_e + (v/v_D)}{1 + (v/v_D)} \quad (1.24\text{bis})$$

with a  $v_D$  of  $17 \text{ m/s}$ .

Figure 4.2  
Fitting for the partition coefficient  $k$

Figure 4.3  
Fit of continuous growth model to silicon-tin partitioning data



# Chapter 5

## Interface Stability in Silicon-Tin

### 5.1 SOS

#### 5.1.1 No indication of breakdown

For low tin doses, the tin and silicon solidified as a supersaturated solid solution. Ion channeling measurements show insignificant levels of non-substitutional tin even though the peak tin concentrations are above the neutral stability curve calculated assuming local equilibrium at the solid-liquid interface. Therefore these samples demonstrate that nonequilibrium effects in rapid solidification stabilize the solid-liquid interface. Table 5-1 and figure 5.1 summarize this data.

Table 5.1  
SOS samples that do not show signs of interface breakdown

tin dose ( $\text{cm}^{-2}$ )	sample	velocity (m/s)	peak concentration (atomic percent)
1e15	6	2.2	0.1
1e15	5	6.3	0.24
1e15	2	7.0	0.24
5e15	3	2.1	0.5
3e15	7	2.5	0.24
5e15	2	2.5	0.5
5e15	1	3.0	0.6
3e15	6	3.3	0.4
3e15	4	4.5	0.7
3e15	3	7.0	0.8
3e15	8	8.3	0.6
8e15	2	8.0	1.0
5e15	7	8.7	1.1
3e15	1	10.	0.9
3e15	2	10.	1.0
8e15	1	11.	2.0
3e15	9	11.	0.8

Figure 5.1  
Interface stability data for SOS: no indication of breakdown

### 5.1.2 RBS and TEM analysis of breakdown

Of the samples for which ion channeling indicated breakdown, we successfully prepared three for cross-sectional transmission electron microscopy. The results are tabulated in table 5.2 and plotted in figure 5.2. The velocity is determined from conductance measurements. The error in velocity is small compared to the size of the symbol in the plot. The concentration is determined by measuring the depth at which cells appear in the cross-sections, then looking at the RBS profile to find the total tin concentration at that depth. For a region of slowly varying concentration, the error is  $\pm 0.1\%$  due to counting statistics.

Table 5.2

RBS and TEM analysis of breakdown for SOS samples:  
critical concentration for interface breakdown as a function of velocity

velocity (m/s)	critical concentration (atomic percent)
2.7	0.32
1.9	1.80
8.6	2.50

Figure 5.2  
Interface stability data for SOS: RBS and TEM analysis of breakdown

Figure 5.3 shows the usefulness of Z-contrast microscopy. The top micrograph is a conventional diffraction contrast in a transmission electron microscope. The micrograph is hard to interpret. The diffraction from defects at the silicon-sapphire interface (the sapphire is the dark gray at the top) give contrast similar to that near the free surface (pointed down). The bottom micrograph is Z-contrast (the free surface is at the top; the sapphire is at the bottom). The dominant features are the tin-rich cell walls.

The sample of figure 5.3 is the low velocity sample. The range of cell wall lengths is much wider than in the other two samples. The transition from totally substitutional tin to mostly non-substitutional tin occurred over a similar range of depths as shown in figure 5.4. The correlation is high, implying that the channeling measurement is sensitive to non-substitutional tin. If the depth where the first cell walls appear is the true point of marginal stability, then the data point moves half way down to the theoretical value. The point plotted in figure 5.2 corresponds to the total tin concentration at the depth where 20% of the cells walls have appeared.

Figure 5.3  
Regular and Z-contrast microscopy for a SOS sample



**Figure 5.4**  
**Analysis of cell wall lengths for a SOS sample**

### 5.1.3 RBS analysis of breakdown (no TEM)

The results for the rest of the SOS samples are tabulated in table 5.3 and plotted in figure 5.5. For the concentration at breakdown, we use the concentration where the total tin concentration and the substitutional tin concentration diverge substantially.

Table 5.3

RBS analysis of breakdown for SOS samples:  
critical concentration for interface breakdown as a function of velocity

velocity (m/s)	critical concentration (atomic percent)
2.0	1.0
4.0	1.2
5.3	1.6
9.0	2.0

Figure 5.5  
Interface stability data for SOS: RBS analysis of breakdown (no TEM)

## 5.2 Bulk Silicon Samples: (100) Orientation

In this section, we present data for samples whose velocities could be determined using the methods of section 3.5. Specifically, there are three cases. First, for samples melted by the XeCl excimer laser without preheating, we use simulation to obtain the velocity as a function of measured melt duration. The relationship between melt duration and velocity is the line plotted in figure 3.19. Second, where the CO<sub>2</sub> and XeCl lasers were used together, we determine the velocity from surface reflectivity and electron microscopy using equation 3.11 and a laser pulse duration of 35 ns. Third, where the Nd:YAG laser was used, we determine the velocity using equation 3.13 and a laser pulse half-duration of 5 ns.

We have already discussed the meaning and uncertainties of the measurements in detail. Now we summarize and calculate error bars. The major contributions to uncertainty in the velocity are spatial non-uniformity of the laser beam and variations from implant to implant in optical coupling. The first effect was measured as  $\pm 4\%$  in fluence, which corresponds to  $\pm 5$  ns for a typical melt. The second effect was measured to be  $\pm 5$  ns as well. Based on repeated melting of clean bulk silicon, the instrumental error for the TDS620 transient digitizer and other parts of the measurement system is negligible. The total uncertainty in melt duration is therefore  $\pm 10$  ns. For a melt duration of moderate length, figure 3.19 shows that an uncertainty of  $\pm 10$  ns translates to an uncertainty in solidification velocity of  $\pm 10\%$ . This is a fair and accurate representation of the relative velocities reported here for the Si(100) samples. An additional factor contributing to uncertainty in the absolute velocities is the thermophysical parameters that go into the heat flow simulations of figure 3.19. This uncertainty is another  $\pm 10\%$  in velocity [Aziz *et al.* 1985]. Thus, we calculate that an error of  $\pm 20\%$  in absolute velocity is fair for all these samples.

Contributions to error in concentration fall into two categories. The first category is how accurately RBS can determine concentrations. The second category relates to interpretation.

First, counting statistics, pile-up, and other errors inherent in spectrometry limit the measurement to  $\pm 0.05$  atomic percent uncertainty in the random spectra and to  $\pm 0.1$  atomic percent in the aligned spectra. The uncertainty is little problem for most of the samples, but is a real limitation on the lowest dose sample. Perhaps the low velocity samples shown in figure 5.1 did undergo breakdown, but we did not see it because we do not have good enough statistics. So what is the ultimate sensitivity of an ion channeling measurement of breakdown? As explained below, breakdown is inferred from the difference between the aligned and random spectra. For a sample that underwent breakdown, an ideal random spectrum might indicate 0.15% and an ideal aligned spectrum 0.07%. However, breakdown would be hidden by the uncertainty of the spectra. Thus, ion channeling is not guaranteed to see breakdown at concentrations lower than 0.2%. The only technique we have for observing breakdown at lower concentrations is cross-sectional electron microscopy.

Second, what are the signs of breakdown in channeling spectra? Consider the sample of figure 5.6. The total tin concentration suddenly rises above the substitutional tin concentration at the same depth where cells appear in the electron micrograph of figure 5.7. This is typical of low dose samples.

Interpretation is much more difficult for high dose samples. The discussion of figure 3.4 (detector resolution effects) showed that the abrupt appearance of non-substitutional tin would be smeared in such a way that calculated substitutional fraction would decrease just before the appearance of cells. Therefore, the channeling spectra will tend to show cells beginning at a deeper depth than microscopy. This is indeed the case for the higher dose samples, such as the one shown in figure 5.15 and 5.16b. When the level of tin is yet higher (figure 5.14 and 5.16a), the divergence of total and substitutional tin is too gradual to be characterized by a single number. In these situations, we take the maximum substitutional concentration as the limit of stability. The error in the measurement is thus larger than the 0.1% error in the RBS alone, and the error varies from sample to sample.

### 5.2.1 RBS and TEM analysis of breakdown

Figures 5.6 through 5.16 show data for these samples. The ion scattering data are presented (one sample per page) first in raw form (top half of the page), then analyzed data (bottom half of the page).

The raw spectra are plotted to show  $\chi$  for both silicon and tin. The drop in yield behind the silicon surface peak in the channeled spectra and the low value of  $\chi$  throughout the silicon show that most of the near surface region is a single-crystal solid solution grown epitaxially on the substrate. Note also that the silicon and tin peaks are unambiguously resolved and that there are no other impurity peaks in between. The indicator of breakdown is a rise in yield in the aligned tin peak.

The analyzed spectra (bottom of page) are plotted to highlight breakdown. The axes are tin concentration as a function of depth in the silicon. The thin line shows as implanted profile measured on a different sample (laser annealing after RBS damages the sample) scaled vertically to give the same area as the total tin profile. The thick line is the total concentration of tin as calculated from the random spectrum. The shaded region is the concentration of substitutional tin calculated using equation 3.2. The indicator of breakdown here is separation between the total concentration and the substitutional concentration.

The electron micrographs are presented as contact prints (two samples per page). The sandwiches were built by placing pieces of the sample face to face. The middle band of the micrograph is the epoxy; pieces of the sample are on either side. Because the pieces are at slightly different orientations, diffraction conditions will be slightly different. It is usually not possible to find a tilt angle that shows cells on both sides of the epoxy. For those samples with boron, the region of dislocation loops appears mottled in contrast with the even gray of the region that melted. Individual loops are too small to be imaged at this magnification. We did not attempt to image individual loops and are relying on Narayan's work [Narayan *et al.* 1983] for the interpretation in terms of dislocation loops.

The two micrographs printed in figure 5.7 (on the page following figure 5.6, the RBS spectra for sample IS10-04-01) are both of

sample IS10-04-01 but are different magnifications. Note that the melt depth and cell formation are uniform across the entire width of the micrograph (2  $\mu\text{m}$ ). Figure 5.10 shows micrograph prints for samples IS04-184 (top) and IS06-075 (bottom). Both prints show the speckled gray below the maximum melt depth; these are the dislocation loops from the boron implant. The print of IS06-075 (bottom) also shows the clean silicon below the boron implant.

Table 5.4 summarizes our interpretation of the micrographs and RBS. The results are plotted in figure 5.17. The data show some scatter. We will discuss the underlying patterns in the next section after presenting more data.

Table 5.4  
RBS and TEM analysis of breakdown for bulk Si(100)

implant & sample	tin dose ( $\text{cm}^{-2}$ )	melt duration (ns)	melt depth ( $\text{\AA}$ )	cell depth ( $\text{\AA}$ )	C (at. %)	V (m/s)	V method
IS11 02.13	3.42e15	286.3	3500	600	0.2	1.4	Eq. 3.11
IS12 02.08	1.36e16	139.0	3200	400	1.05	3.1	Eq. 3.11
IS10 04-01	7.16e15	150.0	4500	410	0.6	3.1	sim. *
IS04 184	3.17e15	142.8	3500	270	0.28	3.2	sim. *
IS03 247	5.29e15	98.3	2300	490	0.43	3.9	sim. *
IS06 075	9.65e15	84.0	2000	330	1.05	4.4	sim. *
IS12 01.20	1.37e16	25	1835	530	1.8	9.0	Eq. 3.13

Column 1 identifies the implant.

Column 2 identifies the sample.

Column 3 is the dose of the tin implant. (Note: all these samples have boron.)

Column 4 is the melt duration measured by surface reflectivity.

Column 5 is the melt depth measured in TEM

Column 6 is the cell depth measured on TEM

Column 7 is the concentration at that depth in RBS

Column 8 is the velocity

An asterisk denotes samples used for the velocity calibration of figure 3.19

Figure 5.6  
RBS and channeling measurements of sample IS10-04-01



**Figure 5.7**  
**Electron micrographs of sample IS10-04-01**  
**5.7a (top): 24000× magnification**  
**5.7b (bottom): 86000× magnification**



Figure 5.8  
RBS and channeling measurements of sample IS04-184



Figure 5.9  
RBS and channeling measurements of sample IS06-075



**Figure 5.10**  
**Electron micrographs of samples**  
**(a) IS04-184: 62500× magnification**  
**(b) IS06-075: 86000× magnification**



Figure 5.11  
RBS and channeling measurements of sample IS03-247



**Figure 5.12**  
**RBS and channeling measurements of sample IS11-02-13**



**Figure 5.13**  
**Electron micrographs of samples**  
**(a) IS03-247: 86000× magnification**  
**(b) IS11-02-13: 105000× magnification**



Figure 5.14  
RBS and channeling measurements of sample IS12-01-20



**Figure 5.15**  
**RBS and channeling measurements of sample IS12-02-08**



**Figure 5.16**

**Electron micrographs of samples**  
**(a) IS12-01-20: 62500× magnification**  
**(b) IS12-02-08: 62500× magnification**



Figure 5.17  
Interface stability data for bulk Si(100) melted with XeCl:  
RBS and TEM analysis of breakdown

### 5.2.2 RBS analysis of breakdown (no TEM): XeCl laser

Table 5.5 presents samples for which we have RBS data but no microscopy data.

Table 5.5

RBS analysis of breakdown for bulk Si(100) samples melted with XeCl laser

implant and sample	tin dose (cm <sup>-2</sup> )	melt duration (ns)	velocity (m/s)	breakdown conc. (atomic %)
IS01 2-01	1.86e16	112.1	3.6	1.2
IS01 2-04	1.87e16	95.4	4.0	1.4
IS01 2-07	1.89e16	89.3	4.2	1.3
IS01 2-15	1.87e16	138.8	3.2	1.1
IS03 055	5.22e15	153.6	3.0	0.45
IS04 033	3.11e15	102.0	3.85	0.28
IS06 111	9.79e15	88.9	4.2	1.05
IS06 100	9.53e15	107.1	3.7	0.95
IS06 084	9.60e15	114.4	3.6	0.9
IS06 252	9.56e15	138.0	3.2	0.8
IS10 4-04	7.26e15	109.2	3.7	0.8
IS10 4-08	7.12e15	98.4	3.9	0.9
IS11 2-02	3.56e15	93.7	4.1	0.4

Column 2 is the dose of the tin implant (all these samples have boron too).

Column 3 is the melt duration measured by surface reflectivity.

Column 4 is the velocity determined from melt duration and simulation.

Column 5 is the critical concentration for breakdown.

### 5.2.3 Combined discussion for samples melted with the XeCl laser

Figure 5.18 plots the data of tables 5.4 and 5.5 (except for the one sample melted by the Nd:YAG laser; we will discuss it in section 5.3).

The data show scatter, but there are some patterns. First, for all samples, the amount of tin in solution exceeds the maximum solubility of tin in silicon, an atomic fraction of  $10^{-3}$  [Massalski, 1986]. Second, all data points

lie well above the local equilibrium neutral stability curve (which is off the bottom of the plot). All the samples have one to two orders of magnitude more tin in solution than the local equilibrium theory predicts.

Nonequilibrium effects strongly stabilize the solid-liquid interface. The nonequilibrium theory has at least some merit because it does predict the large increase in breakdown concentration.

The third observation is that most data points lie above the neutral stability curve. This is consistent with a solute gradient and delayed evidence of breakdown. We quantify the concentration gradient by looking at how much the total tin concentration increased in the 1000 Å leading up to breakdown. The data of figure 5.18 are grouped according to the gradient, with the circles representing the lowest gradient and the diamonds representing the highest. The higher the gradient, the further the data points deviate from what theory predicts. The samples with low concentration gradients agree well with the theory. This is expected because low gradients offer the best approximation of steady-state solidification as assumed in the theory.

Figure 5.18  
Interface stability data for bulk Si(100) melted with XeCl:  
RBS analysis of breakdown (some TEM);  
the solute gradient effect

### 5.3 RBS Analysis of Breakdown: Nd:YAG Laser

First, we verify that we can usefully simulate pulsed laser melting of bulk silicon with the Nd:YAG laser. Cross-sectional transmission electron microscopy of one sample indicates that for a melt duration of 25 ns, the melt depth is 1835 Å and hence (using equation 3.13) that the solidification velocity is 9 m/s. Simulations of 1300 Å amorphous silicon on bulk silicon melted with a Nd:YAG laser say that a 25 ns melt corresponds to a 1470 Å melt depth and a solidification velocity of 8.7 m/s. The 20% error in maximum melt depth is not surprising. The calculation is sensitive to the temporal profile of the laser pulse, and the Nd:YAG pulse changes profile each shot. The three profiles of figures 2.9 and 2.10 give maximum melt depths that differ by 5%. An uncertainty in melt duration of  $\pm 1$  ns accounts for another 10%. Therefore, the agreement between simulated and measured maximum melt depth is satisfactory. The 3% error in velocity is fortuitous. As noted in section 2.3.3, the spatial profile of the Nd:YAG pulse is such that the velocity varies by  $\pm 1$  m/s over the area of the sample. On the whole, this data point is a promising indicator for quantitative simulation. We have two reservations. First, it is but a single datum. Second, it is at the low end of the measured melt durations and not near the middle of the data.

We analyze the rest of the Nd:YAG data by doing a series of simulations and making a table of solidification velocity as a function of melt duration (in the manner of figure 3.19). The results for neutral stability are given in table 5.6 and figure 5.19. There is again scatter in the data, but given the size of the error bars, the data are consistent with the predictions. The sample for which microscopy results are available happens to be the datum that agrees best with theory.

Table 5.6:  
RBS analysis of breakdown for bulk Si(100) melted with Nd:YAG

implant & sample	melt duratio n ns	V m/s	C at %	tin dose
10	01-17	31.3	7.3	1.1 medium
11	01-08	30.7	7.4	0.6 low
11	01-12	28.3	7.9	0.6 low
10	01-18	27.3	8.1	1.0 medium
12	01-20	24.6	* 8.7	1.8 high
12	01-05	23.1	9.1	0.8 high
12	01-25	22.3	9.3	1.8 high
10	01-19	20.7	9.7	1.1 medium

\* Microscopy (figure 5.16a) indicates a melt depth of 1835 Å, hence a velocity of 9 m/s.

Figure 5.19  
Interface stability data for bulk Si(100) melted with Nd:YAG:  
RBS analysis of breakdown (one TEM sample)

## 5.4 Bulk Silicon Samples: (111) Orientation

Solute trapping studies of Si(111) [Reitano *et al.* 1994] give a diffusive velocity of 5.1 m/s for silicon-tin. This is substantially lower than the 17 m/s for Si(100). Therefore for a given (high) velocity, the interface is more stable. Table 5.7 shows the results of our measurements, and figures 5.20 through 5.22 show RBS and microscopy data for two samples. Figure 5.23 compares the results to the theory. (The parameters for the calculation are those given in table 2.1, including the orientationally averaged surface tension of 0.36 J/m<sup>2</sup>). As with the Si(100) data, the quantitative agreement is good. Several qualitative features are repeated. The (111) data are more than two orders of magnitude higher in concentration than predicted by the local equilibrium theory (which is off the bottom of the graph). Also, the lower implant doses are a better match to the theory than the higher doses. This is because a lower dose results in a lower solute gradient.

We have nearly the same confidence in the velocities of the (111) samples as the (100) samples. The difference in orientation will not change the thermophysical properties, nor will it have a noticeable effect on the optical properties at the wavelength of the XeCl laser (308 nm). The only additional source of uncertainty is the extremely high doses of tin. The SOS samples with this level of implantation gave strange conductivity signals, but we needed the high doses for these samples because of the increased trapping. Also, none of the samples had boron, so we cannot use microscopy and equation 3.11 to check the dose effect. We estimate the uncertainty by examining the variation in melt duration as a function of fluence observed for the different implants. Looking at the scatter for the Si(111) samples plotted in figure 3.17b (the circles, triangles, and crosses), the variation with dose is more important than for the Si(100) samples shown in figure 3.17a. This variation increases the error bars by 3% to  $\pm 13\%$  for relative velocity and  $\pm 23\%$  for absolute velocity.

Table 5.7:  
Interface Stability for Si(111)

implant & sample		tin dose (cm-2)	melt duration (ns)	velocity (m/s)	critical conc. (at. %)	TEM figure
1	3	8.85e15	125.0	3.4	0.95	
1	4	9.18e15	109.6	3.7	1.1	
2	28	1.83e16	128.7	3.4	1.6	5.22a
2	41	1.83e16	166.3	2.8	1.7	
2	46	1.83e16	99.2	3.9	1.8	
4	7	3.41e16	138.2	3.2	1.9	
4	9	3.51e16	109.2	3.7	1.6	
4	10	3.45e16	166.4	2.8	1.9	*

Column 1 identifies the implant (111Sn\_ in table 2.2) and the sample

Column 2 is the tin dose measured in RBS

Column 3 is the melt duration measured by surface reflectivity

Column 4 is the velocity determined from melt duration and simulation

Column 5 is the critical concentration for interface breakdown

\* verified breakdown in TEM, but no micrograph is shown

Figure 5.20  
RBS and channeling measurements of sample 111-2-028



Figure 5.21  
RBS and channeling measurements of sample 111-4-010



Figure 5.22  
Electron micrographs of sample  
(a) 111-2-028: 86000 $\times$  magnification



Figure 5.23  
Interface stability data for bulk Si(111) melted with XeCl:  
RBS analysis of breakdown (two TEM samples)

## 5.5 Bulk Silicon Samples: Cell Size

Because linear stability theory examines the effect of a single Fourier component, there is some information about cell size. Cells however are not infinitesimal perturbations of the solid-liquid interface. Non-linear stability theory and pattern selection theory address the dynamics of instability growth. However, we know of no calculation of cell size for rapidly solidified silicon-tin in that literature. Therefore, we will compare our result to a calculation by Brunco [Brunco, 1995] for a sample solidified at 2 m/s.

We prepared one sample for plan-view transmission electron microscopy. It was a bulk Si(100) sample implanted with  $1e16 \text{ cm}^{-2}$  tin and melted with a XeCl excimer pulse. The melt duration was 130 ns melt, implying a solidification velocity of 3.4 m/s. Figure 5.24 is a micrograph of the sample. The sample has a clear and regular cellular structure. The characteristic cell size is 60 nm compared to Brunco's calculation of 235 nm.

We have successfully prepared a dozen samples for cross-sectional transmission electron microscopy. A good approximation of the cell size for those samples is the largest commonly observed spacing between cell walls. Looking at these samples, we conclude that they are consistent with the plan-view sample, and that cell size is not a strong function of velocity over the range available to us.

Figure 5.24  
Plan-view TEM showing cellular structure

# Chapter 6

## Conclusions

We have made quantitative measurements of solute trapping in the silicon-tin system for the (100) orientation. Solidification velocities were measured by transient conductance, and solute profiles by RBS. The data were well fit by a liquid diffusivity of  $2.5 \times 10^{-4}$  cm<sup>2</sup>/s and by the continuous growth model with a diffusive velocity of 17 m/s.

For both (100) and (111) orientations, we have also studied the stability of the planar interface during rapid solidification by searching for the limits of solid solution formation. When the concentration exceeded the solubility limit, the sample microstructure becomes cellular. Typical cell size was 600 Å.

To measure velocity, we used three techniques. The first was direct: conductance measurements on SOS samples. Looking at these measurements, we noted that the samples started to solidify when the laser pulse ended and that the solidification velocity was nearly constant. This inspired the second technique where we calculated velocity using the rule

$$\text{velocity} = \frac{\text{maximum melt depth}}{\text{time between end of laser pulse and end of solidification}} \quad (6.1)$$

The calculation required three measurements: the laser pulse temporal

profile, the surface melt duration (from surface reflectivity), and the maximum melt depth (from observation of a marker layer in cross-sectional electron microscopy). This technique confirmed the third technique, heat flow simulation, for bulk silicon samples that were at room temperature before firing the melting laser. Figure 6.1 shows the simulated velocity as a function of melt duration for bulk-silicon samples with an amorphous surface layer melted with the XeCl excimer laser (figure 6.1a) and with the Nd:YAG laser (figure 6.1b). The error bars shown are those calculated in chapter 5. The agreement is good, especially for the XeCl samples. Therefore, simulation is a reliable method for calculating the solidification velocities for these samples.

We found that nonequilibrium solidification effects substantially stabilize the solid-liquid interface, and the result could be quantitatively calculated using linear stability theory without resort to adjustable parameters. Figure 6.2 combines the data of figures 5.1, 5.2, 5.5, and 5.17. The agreement is very good when two conditions are simultaneously met. First, the dose of the tin implant should be low enough that the interface just reaches the critical concentration for breakdown. Second, the melt duration should be long enough that the melt and the solid-liquid interface can reach steady-state.

Figure 6.2 shows two theory curves. Both curves correspond to the theory presented in section 1.3.2 using a simple method that gives only the result for neutral stability against steady instabilities as calculated by Huntley and Davis [Huntley and Davis, 1993a]. The solid line corresponds to a surface tension of  $0.36 \text{ J/m}^2$  [Evans and Stiffler, 1991], the value used by Huntley and Davis [Huntley and Davis, 1993a] and Brunco [Brunco, 1995]. The dashed curve corresponds to a surface tension of  $0.45 \text{ J/cm}^2$  [Shao and Spaepen, 1995]. Both curves fit the data equally well. The theory of Brunco [Brunco, 1995] is not plotted, but it fits the data as well. Huntley and Davis's and Brunco's theories make similar predictions in the region of concentration-velocity space explored by this experiment because the concentrations are low (dilute solution regime) and the velocities are always smaller than the diffusive velocity. Given the size of the error bars, we cannot say that any theory fits better than any other. All theories account for the major features of nonequilibrium interface stability.

Figure 6.1  
Comparison of measured and simulated solidification velocities



Figure 6.2  
Master plot of interface stability experiments in Si(100)



# Appendix A: Modifications to SA

We modified Patrick Smith's SA program [Smith, 1992] to do channeling analysis. This appendix gives new and revised sections of the users manual.

## 4.4.2 Substitutional Fraction Calculation Using Channeled Spectra

Rutherford backscattering is a low probability, high angle event. Particles of the beam also experience high probability, low angle scattering as they interact with the screened Coulomb field of the target atoms. If the beam is incident on a crystal along a low-index direction, beam particles interact with the target almost as if the rows and planes of atoms blurred into a charge continuum. The lines and planes of charge gently steer beam particles away from the target atoms and so decrease the odds of a backscattering event. This effect is called channeling. When a clean, high quality crystal is well aligned with the beam, the backscattering yield drops dramatically.

Small concentrations of a substitutional impurity have almost no effect on the channeling properties of the host lattice. Non-substitutional impurities have a large effect; they can completely block channels through the host lattice. The change in scattering yield reveals something about the position of impurity atoms relative to the host lattice.

The goal here is to calculate the fraction  $S$  of impurity atoms that is substitutional. The algorithm is an extension of the one described at the end of chapter two of *Materials Analysis by Ion Channeling* by Feldman, Mayer, and Picraux. The same limitations apply: it is rigorously valid only “for a mixed site case in which a fraction  $S$  [of the impurity] is substitutional and the remainder occupies a random distribution of sites.” The assumption of SA’s extended algorithm is that the channeled spectrum is perfectly aligned and that the random spectrum is free of all channeling affects. Moreover, the counting statistics must be good enough for channel by channel comparison.

The calculation proceeds as follows. The first step is to quantify the effect of channeling. This is  $\chi$ , which equals the counts in each channel of the channeled spectrum divided by the counts in the same channel of the random spectrum. This gives  $\chi$  as a function of channel. This is converted to  $\chi$  as a function of depth for the substrate and the impurity using depth scale information. The substitutional fraction is then

$$S = (1 - \chi_{imp}) / (1 - \chi_{sub}) \quad (4.26)$$

(equation 2.29 of Feldman, Mayer, and Picraux). If the impurity atoms obstruct channeling, then the counts in the impurity peak of the channeled spectrum would be more like the counts in the random spectrum, so  $\chi_{imp}$  would be larger. Therefore,  $S$  would be smaller. If all impurity atoms were substitutional, there would still be some dechanneling, but no more than the dechanneling seen in the substrate. Therefore,  $\chi_{imp}$  would equal  $\chi_{sub}$ , and  $S$  would be one.

This calculation requires a channeling spectrum and a random spectrum. Because the algorithm assumes that a fixed channel represents scattering from the same element at the same depth in both spectra, the spectra must have the same energy calibration and experimental parameters.

The channeling analysis is an optional switch on the impurity command. The command syntax requires you to specify either the random or the channeled spectrum; the active spectrum is assumed to be the other. If SA sees that you have specified either one, it will calculate an impurity depth concentration profiles for the random spectrum and calculate substitutional fraction as a function of depth. The profile calculated from the random spectrum

is the usual impurity calculation. It gives the total impurity concentration as a function of depth.

When the substitutional fraction calculation is performed, two depth profiles will be display on the depth profile screen. The first will be the depth profile calculated from the random spectrum. The second will be the non-substitutional profile, actually the product of  $1-S$  and the depth profile from the random spectrum.

If `IMPURITY` is writing depth profiles to disk files (if `SET IMPFILES` is ON), then `IMPURITY` will create only one output file with the substitutional fraction calculation is performed. The file created will have the same filename as the random spectrum, with the usual element name extension. However, a fifth column is added to the file containing the substitutional fraction.

See page 8-17 for a description of the `IMPURITY` command options used to perform the substitutional fraction calculation.

The output consists of two depth profiles. The first is always the total concentration. On the screen, the second is the non-substitutional profile, actually the product of  $1-S$  and the total impurity concentration. In the output file, the second profile (the third or fifth column of the file) is the substitutional fraction.

## Appendix B: Silicon Properties used in Heat Flow Simulations

thermophysical property	liquid	amorph.	crystal
melting temperature (K)		1430	1685
latent heat of fusion (J/cm <sup>3</sup> )		2986	4206
Kinetic undercooling ((m/s)/K)		0.267	0.0667
optical reflectivity at 308nm	0.734	0.562	0.587
optical reflectivity at 1064 nm	0.777	0.4	0.32
optical absorption at 308nm (1/cm)	1.53e6	1.38e6	1.48e6
optical absorption at 1064nm (1/cm)	0.86e6	1.e5	2000
Thermal conductivity (W/(K·cm))	1.4	0.026	

### References

Melting temperature	Hultgren <i>et al.</i> 1973
Latent heat of melting of crystal	Touloukian, 1970
Latent heat of melting of amorphous	Donovan <i>et al.</i> 1983
optical properties at 308nm	Jellison, 1984
optical properties at 1064 nm	Palik, 1991
thermal conductivity of liquid	Ho <i>et al.</i> 1971
thermal conductivity of amorphous	Papa <i>et al.</i> 1983

Properties that are a function of temperature

Temperature	Specific Heat (all phases)	Temperature	Thermal Conductivity (crystal)
K	J/(K.cm <sup>3</sup> )	K	W/(K.cm)
273	1.609	273	1.68
		300	1.48
		350	1.19
373	1.794	400	0.989
473	1.920	500	0.762
573	1.974	600	0.619
673	2.013	700	0.508
773	2.052	800	0.422
873	2.091	900	0.359
973	2.125	1000	0.312
1073	2.159	1100	0.279
1173	2.193	1200	0.257
1273	2.232	1300	0.244
1373		1400	0.235
1500	2.367	1500	0.227
1600	2.392	1600	0.221
1690	2.414	1685	0.220
1800	2.461		
1900	2.482		

Thermal conductivity of crystalline silicon from [Ho *et al.* 1971].

Specific heat of silicon from [Touloukian, 1970]. The data were originally tabulated in cal/(g·K); we converted to J/(K·cm<sup>3</sup>) using 2.33g/cm<sup>3</sup> and 4.184J/cal

# References

[Aziz and Kaplan, 1988]

Continuous growth model for interface motion during alloy solidification. M.J. Aziz and T. Kaplan. *Acta Metallurgica*, vol.26, no.8, p.2335 (1988).

[Aziz *et al.* 1985]

Melting of crystalline and amorphous silicon by ruby, XeCl and KrF laser irradiation. M.J. Aziz, C.W. White, J. Narayan, and B. Stritzker. *Energy Beam-Solid Interaction and Transient Thermal Processing IV* (Editions de Physique, France), p.231 (1985).

[Aziz *et al.* 1986]

Solute trapping: comparison of theory with experiment. M.J. Aziz, M.O. Thompson, P.S. Peercy, and C.W. White. *Physical Review Letters*, vol.56, no.23, p.2489 (1986).

[Baeri *et al.* 1980]

Dependence of trapping and segregation of indium in silicon on the velocity of the liquid solid interface. P. Baeri, J.M. Poate, S.U. Campisano, G. Foti, E. Rimini, A.G. Cullis. *Applied Physics Letters*, vol.37, no.10, p.912 (1980).

[Baker and Cahn, 1969]

Solute trapping by rapid solidification. J.C. Baker and J.W. Cahn. *Acta Metallurgica*, vol.17, p. 575 (1969).

[Baker and Cahn, 1971]

J.C. Baker and J.W. Cahn. In *Solidification* (American Society for Metals, Metals Park, Ohio, 1971), p.21 (1971).

[Boettinger *et al.* 1984]

The effect of rapid solidification velocity on the microstructure of Ag-Cu alloys. W.J. Boettinger, D. Shechtman, R.J. Schaefer, F.S. Biancaniello. *Metallurgical Transactions A*, vol.15, p.55 (1984).

[Boettinger *et al.* 1988]

Application of dendritic growth theory to the interpretation of rapid solidification microstructures. W.J. Boettinger, S.R. Coriell, and R. Trivedi. In *Rapid Solidification Processing: Principles and Technologies, IV*; p.13. Edited by R. Mehrabian and P.A. Parrish (Claitor's Publishing Division, Baton Rouge, Louisiana), 1988.

[Brunco, 1995]

Nonequilibrium solidification of nondilute alloys: Measurements in GeSi alloys and extensions of interface stability theory. D.P. Brunco, PhD Thesis, Cornell University, 1995.

[Campisano and Poate, 1985]

Velocity dependence of maximum substitutional concentrations of In and Bi trapped in rapidly solidified Si. S.U. Campisano and J.M. Poate. *Applied Physics Letters*, vol.47, no.5, p.485 (1985).

[Carrard *et al.* 1992]

About the banded structure in rapidly solidified dendritic and eutectic alloys. M. Carrard, M. Gremaud, M. Zimmermann, and W. Kurz. *Acta metall. mater.* vol.40, no.5, p.983 (1992).

[Coriell and Sekerka, 1983]

Oscillatory morphological instabilities due to non-equilibrium

segregation. S.R. Coriell and R.F. Sekerka. *Journal of Crystal Growth*, vol.61, no.3, p.499 (1983).

[Cullis et al, 1981]

Growth interface breakdown during laser recrystallization from the melt. A.G. Cullis, D.T.J. Hurle, H.C. Webber, N.G. Chew, J.M. Poate, P. Baeri, and G. Foti. *Applied Physics Letters*, vol.38, no.5, p. 642 (1981).

[Donovan *et al.* 1983]

Heat of crystallization and melting point of amorphous silicon. E.P. Donovan, F. Spaepen, D. Turnbull, J.M. Poate, and D.C. Jacobson. *Applied Physics Letters*, vol.42, no.8, p.698 (1983).

[Evans and Stiffler, 1991]

Interfacial atomic transport in the nucleation of crystalline silicon from the melt. P.V. Evans and S.R. Stiffler. *Acta Metall.* vol.39, no.11, p.2727 (1991).

[Feldman *et al.* 1982]

L.C. Feldman, J.W. Mayer, and S.T. Picraux. *Materials Analysis by Ion Channeling*. Academic Press, New York (1982).

[Gibson, 1960]

*Progress in Semiconductors*, vol.4. Edited by A.F. Gibson. J. Wiley, New York (1960).

[Ho *et al.* 1971]

Thermal Conductivity of the Elements: A Comprehensive Review. C.Y. Ho, R.W. Powell, and P.E. Liley. *Journal of Physical and Chemical Reference Data*, vol.3, suppl.1 (1971).

[Hoglund *et al.* 1991]

Effect of nonequilibrium interface kinetics on cellular breakdown of planar interface during rapid solidification of Si-Sn. D.E. Hoglund, M.J. Aziz, S.R. Stiffler, M.O. Thompson, J.Y. Tsao, and P.S. Peercy. *Journal of Crystal Growth*, vol.109, p.107 (1991).

- [Hoglund and Aziz, 1992]  
Interface stability during rapid solidification. Materials Research Society Symposium Proceedings, vol.205, p.325 (1992).
- [Hultgren *et al.* 1973]  
Selected Values of the Thermodynamic Properties of the Elements. Edited by R. Hultgren, P.D. Desai, D.T. Hawkins, M. Gleiser, K.K. Kelley, and D.D. Wagman. American Society for Metals, Metals Park, Ohio (1973).
- [Huntley and Davis, 1993a]  
Thermal effects in rapid direction solidification: Linear theory. D.A. Huntley and S.H. Davis, Acta Metall. Mater. vol.41, no.7, p.2025 (1993).
- [Huntley and Davis, 1993b]  
Thermal effects in rapid directional solidification: weakly-nonlinear analysis of oscillatory instabilities. D.A. Huntley and S.H. Davis, Journal of Crystal Growth, vol.132, p.141 (1993)
- [Jellison *et al.* 1981]  
Optical properties of heavily doped silicon between 1.5 and 4.1 eV. G.E. Jellison, F.A. Modine, C.W. White, R.F. Wood, and R.T. Young. Physical Review Letters, vol.46, no.21, p.1414.
- [Jellison, 1984]  
G.E. Jellison, Jr. In Semiconductors and Semimetals, eds. R.K. Willardson and A.C. Beer, chapter 3 in volume 23: *Pulsed Laser Processing of Semiconductors*, eds. R.F. Wood, C.W. White, and R.T. Young. Academic Press, New York (1984).
- [Karma and Sarkissian, 1993]  
Interface dynamics and Banding in Rapid Solidification. A. Karma and A. Sarkissian. Physical Review, vol.E47, p.513 (1993).
- [Kramer *et al.* 1992]  
Crystallinity, strain, and thermal stability of heteroepitaxial Si<sub>1-x</sub>Ge<sub>x</sub>/Si (100) layers created using pulsed laser induced epitaxy. K.-J. Kramer, S.

Talwar, T.W. Sigmon, and K.H. Weiner. *Applied Physics Letters*, vol. 61, no.7, p.769 (1992).

[Langer and Müller-Krumbhaar, 1978]

Theory of dendritic growth — I, II, III. J.S. Langer and H. Müller-Krumbhaar. *Acta Metallurgica*, vol.26, no.11, pp.1681ff, (1978).

[Lombardo *et al.* 1991]

S. Lombardo, K. Kramer, M.O. Thompson, and D.R. Smith. *Applied Physics Letters*, vol.59 (1991).

[MacDonald *et al.* 1989]

Picosecond time-resolved measurements of crystallization in noble metals. C.A. MacDonald, A.M. Malvezzi, and F. Spaepen. *Journal of Applied Physics*, vol.65, no.1, p.129 (1989).

[Massalski, 1986]

*Binary Alloy Phase Diagrams*. Edited by T.B. Massalski. American Society for Metals, Metals Park, OH (1986).

[Mayer and Lau, 1972],

J.W. Mayer and S.S. Lau. *Electronic Materials Science: For Integrated Circuits in Si and GaAs*. Macmillan, New York (1972).

[Merchant and Davis, 1990]

Morphological instability in rapid directional solidification. G.J. Merchant and S.H. Davis, *Acta Metall. Mater.* vol.38, p.2683 (1990).

[Morris and Winegard, 1969]

The development of cells during solidification of a dilute Pb-Sb alloy. L.R. Morris and W.C. Winegard. *Journal of Crystal Growth*, vol.5, p.361 (1969).

[Mullins and Sekerka, 1964]

Stability of a planar interface during solidification of a dilute binary alloy. W.W. Mullins and R.F. Sekerka. *Journal of Applied Physics*, vol.35 no.2, p.444 (1964).

[Narayan, 1982]

Development of morphological stability and formation of cells in silicon alloys during pulsed laser irradiation. J. Narayan. *Journal of Crystal Growth*, vol.59, p.583 (1982).

[Narayan *et al.* 1983]

Excimer laser annealing of ion-implanted silicon. J. Narayan, O.W. Holland, C.W. White, and R.T. Young. *Journal of Applied Physics*, vol.55, no.4, p.1125 (1984).

[Palik, 1991]

*Handbook of optical constants of solids II*. Edited by E.D. Palik. Academic Press, Boston (1991).

[Papa *et al.* 1983]

T. Papa, F. Scudieri, M. Marinelli, U. Zammit, and G. Cembali. *J.Phys. (Paris) Colloq.C5*, p.73 (1983).

[Pennycook and Narayan, 1984]

Direct imaging of dopant distribution in silicon by scanning transmission electron microscopy. S.J. Pennycook and J. Narayan. *Applied Physics Letters*, vol.45, no.4, p.385 (1984).

[Pennycook, 1989]

High-resolution imaging with large-angle elastically scattered electrons. S.J. Pennycook. *EMSA Bulletin*, vol.19, no.1, p.67 (1989).

[Reitano *et al.* 1994]

Solute trapping of group III, IV, and V elements in silicon by an aperiodic stepwise growth mechanism. R. Reitano, P.M. Smith, and M.J. Aziz. *Journal of Applied Physics* vol.76, no.3, p.1518 (1994).

[Sekerka, 1967]

A stability function for explicit evaluation of the Mullins-Sekerka interface stability criterion. R.F. Sekerka. *Journal of Applied Physics* vol.36, no.1, p.264 (1967).

[Shao and Spaepen, 1995]

Undercooling of bulk liquid silicon in an oxide flux. Y. Shao and F. Spaepen. Submitted to Journal of Applied Physics, 1995.

[Smith, 1992]

*Solute Trapping in Aluminum Alloys*. Patrick Smith, PhD thesis, Harvard University, 1992.

[Smith and Aziz, 1994]

Solute trapping in aluminum alloys. P.M. Smith and M.J. Aziz. *Acta Metall. Mater.* vol.42, no.10, p.3515 (1994).

[Thurmond and Kowalchik, 1960]

C.D. Thurmond and M. Kowalchik. *Bell System Technical Journal* vol.39, p.169 (1960).

[Tiller 1984]

Foreword: Quantitative solidification science. W.A. Tiller. *Material Science and Engineering*, vol.65, no.1 (Special issue on solidification microstructure: 30 years after constitutional supercooling) p.3 (1984).

[Tiller, Jackson, Rutter, and Chalmers, 1953]

The redistribution of solute atoms during the solidification of metals. W.A. Tiller, K.A. Jackson, R.W. Rutter, and B. Chalmers. *Acta Metallurgica*, vol.1, p.428 (1953).

[Touloukian, 1970]

Thermophysical properties of matter: the Thermophysical Properties Research Center data series. Y. S. Touloukian, series editor. IFI/Plenum, New York, 1970-79.

See Thermal Conductivity of Nonmetallic Solids, p.339.

See Specific Heat, p.205.

[Trivedi and Kurz, 1986]

Morphological stability of a planar interface under rapid solidification conditions. R. Trivedi and W. Kurz. *Acta Metallurgica*, vol.38, no.8, p.1663 (1986).

[van Saarloos, 1988]

Front propagation into unstable states: Marginal stability as a dynamical mechanism for velocity selection. W. van Saarloos. *Physical Review A*, vol.37, no.1, p.211 (1988).

[White *et al.* 1980]

Supersaturated substitutional alloys formed by ion implantation and pulsed laser annealing of group-III and group-V dopants in silicon. C.W. White, S.R. Wilson, B.R. Appleton, F.W. Young, Jr. *Journal of Applied Physics*, vol.51, no.1, p.738 (1980).

[Winegard and Chalmers]

W.C. Winegard and B. Chalmers. Cited in [Tiller, Jackson, Rutter, and Chalmers, 1953] as “to be published.”

[Wollkind and Segel, 1970]

A nonlinear stability analysis of the freezing of a dilute binary alloy. D.J. Wollkind and L.A. Segel. *Philosophical Transactions of the Royal Society of London*, vol.268A, p.1191 (1970).